Burial and exhumation in a subduction wedge : mutual constraints from thermo-mechanical modelin and natural P-T-t data (Sch. Lustrés, W. Alps)

P. Yamato, Philippe Agard, Evgenii E.B. Burov, Latetia Le Pourhiet, Laurent Jolivet, Christel Tiberi

Burial and exhumation in a subduction wedge: Mutual constraints from thermomechanical modeling and natural P-T-t data (Schistes Lustrés, western Alps)

P. Yamato,[1] P. Agard,[1] E. Burov,[1] L. Le Pourhiet,[1] L. Jolivet,[1] and C. Tiberi[1]

Received 11 April 2006; revised 17 January 2007; accepted 12 February 2007; published 19 July 2007.

[1] The dynamic processes leading to synconvergent exhumation of high-pressure low-temperature (HP-LT) rocks at oceanic accretionary margins, as well as the mechanisms maintaining nearly steady state regime in most accretion prisms, remain poorly understood. The present study aims at getting better constraints on the rheology, thermal conductivity, and chemical properties of the sediments in subduction zones. To reach that goal, oceanic subduction is modeled using a forward visco-elasto-plastic thermomechanical code (PARA(O)VOZ-FLAC algorithm), and synthetic pressure-temperature-time (P-T-t) paths, predicted from numerical experiments, are compared with natural P-T-t paths. The study is focused on the well constrained Schistes Lustrés complex (SL: western Alps) which is thought to represent the fossil accretionary wedge of the Liguro-Piemontese Ocean. For convergence rates comparable to Alpine subduction rates ($\sim$3 cm yr^{-1}), the best-fitting results are obtained for high-viscosity, low-density wedge sediments and/or a strong lower continental crust. After a transition period of 3–5 Ma the modeled accretionary wedges reach a steady state which lasts over 20 Ma. Over that time span a significant proportion ($\sim$35%) of sediments entering the wedge undergoes P-T conditions typical of the SL complex ($\sim$15–20 kbar; 350–450°C) with similar P-T loops. Computed exhumation rates (<6 mm yr^{-1}) are in agreement with observations (1–5 mm yr^{-1}). In presence of a serpentinite layer below the oceanic crust, exhumation of oceanic material takes place at rates approaching 3 mm yr^{-1}. In all experiments the total pressure in the accretionary wedge never deviated by more than ±10% from the lithostatic component.

Citation: Yamato, P., P. Agard, E. Burov, L. Le Pourhiet, L. Jolivet, and C. Tiberi (2007), Burial and exhumation in a subduction wedge: Mutual constraints from thermomechanical modeling and natural P-T-t data (Schistes Lustrés, western Alps), *J. Geophys. Res.*, *112*, B07410, doi:10.1029/2006JB004441.

1. Introduction

[2] Petrological studies of successive mineralogical assemblages found in metamorphic rocks allow, in principle, the reconstruction of their pressure-temperature evolution and the assessment of pressure-temperature-time paths (P-T-t paths) [e.g., *Spear*, 1993; *Müller*, 2003]. These studies provide ideal constraints for models of exhumation in accretionary subduction wedges [e.g., *Cloos*, 1982; *Shreve and Cloos*, 1986; *Brandon et al.*, 1998]. However, despite recent progress in assessment of P-T-t trajectories [*Berman*, 1991; *Holland and Powell*, 1998; *Vidal and Parra*, 2000] and uplift rates [e.g., *Gunnell*, 2000; *Zeitler et al.*, 2001], our knowledge of the vertical trajectories remains fragmentary [e.g., *Duchêne et al.*, 1997a]. Indeed, prograde P-T-t paths are often largely overprinted because of reequilibrations with rising temperature, and the retrograde parts are often preserved as discrete reequilibration steps only [*Spear*, 1993; *Jolivet et al.*, 2003]. P-T-t paths therefore represent only a partial record of vertical trajectories, and much of the information related to burial is lost. Moreover, P-T-t paths are not univocally interpretable in terms of geodynamic settings either. It is therefore useful to compare the natural P-T-t paths with synthetic ones obtained from thermomechanical modeling in order to clarify burial/exhumation and geodynamic processes, and explore their dependence on the parameters such as the convergence rate or the intrinsic properties of the accretionary wedge.

[3] Following the approach of Gerya and coworkers [e.g., *Gerya et al.*, 2002, 2006; *Vasilyev et al.*, 2004; *Stöckhert and Gerya*, 2005], we include the effects of metamorphic phase changes on density, and trace the predicted P-T-t paths within the models using passive markers. The main difference of our approach is that we account for the effective elasto-plastic behavior of the rocks constituting the accretionary wedge and the entire lithosphere, for

[1]Laboratoire de Tectonique, UMR CNRS 7072, Université Paris 6, Paris, France.

0148-0227/07/2006JB004441$09.00

example, the transition from brittle behavior (Mohr-Coulomb plasticity) to ductile viscous effective behavior at temperatures higher than 300°C. Hence we have chosen to use an explicit thermomechanical code (PARA(O)VOZ) [e.g., *Poliakov et al.*, 1993] that allows for strongly nonlinear visco-elasto-plastic behaviors. Another important feature of our models is that the kinematic boundary conditions are imposed at the lateral borders of the model and not on the subducting plate itself, allowing the slab to deform freely in response to the formation of the accretionary wedge.

[4] Owing to the wealth of petrology data and the abundance of published P-T-t paths (Figure 1) [e.g., *Ernst and Dal Piaz*, 1978; *Van der Klauw et al.*, 1997; *Reinecke*, 1998; *Messiga et al.*, 1999; *Schwartz et al.*, 2000a; *Agard et al.*, 2001, 2002], the western Alps constitute a good natural example to test the kinematics of our models. We first review the main P-T-t data coming from the western Alps (focusing on the oceanic units) and the geodynamic context of formation of the Alpine belt. We then present the results of our numerical experiments and discuss the influence of various physical parameters on the shapes of P-T-t paths, and compare the synthetic P-T-t paths and exhumation rates with natural ones. This study, though focusing on the subduction of the Liguro-Piemontese Ocean, is also relevant for other accretionary wedges as, for example, the Franciscan Complex (western United States).

2. Geological Setting

2.1. Geodynamic Context and Significance of the Schistes Lustrés Complex

[5] The western Alps result from the closure of the Valais and Liguro-Piemontese oceans, and further information on paleogeography and geodynamics can be found in numerous reviews [e.g., *Le Pichon et al.*, 1988; *Coward and Dietrich*, 1989; *Stampfli et al.*, 1998; *Oberhänsli et al.*, 2004]. Subduction of the ~800–1000 km wide Liguro-Piemontese Ocean [*Lemoine et al.*, 1986; *Lemoine and Tricart*, 1986; *Dercourt et al.*, 1993] occurred from ~100 Ma onward through an E-dipping subduction (as shown by the metamorphic zoneography; Figure 1a) at slow convergence rates (<20 mm yr^{-1}; [*Le Pichon et al.*, 1988; *Lapen et al.*, 2003]). The final closure of this ocean is dated at ~45 Ma [*Deville et al.*, 1992; *Michard et al.*, 1996; *Rosenbaum and Lister*, 2005].

[6] Metamorphic rocks reached depths ranging from 30 to 100 km [e.g., *Goffé and Chopin*, 1986; *Chopin*, 2003] and were fortunately little overprinted by later collision in the western Alps [*Gillet and Goffé*, 1988; *Chopin et al.*, 1991]. Eclogites are found in the oceanic Zermatt-Saas and Monviso units, and in the continental Dora Maira, Gran Paradiso, and Sesia massifs (Figure 1) [*Chopin*, 1984; *Philippot and Kienast*, 1989; *Pognante*, 1991; *Lardeaux and Spalla*, 1991; *Spalla et al.*, 1996; *Van der Klauw et al.*, 1997; *Reinecke*, 1998], whereas blueschist facies conditions prevail in the Briançonnais and in the Schistes Lustrés complex [*Goffé and Velde*, 1984; *Agard et al.*, 2001]. The gradual increase of P-T conditions in the latter unit allowed the recognition of the SL complex as representing a fossil accretionary wedge [*Agard et al.*, 2001; *Schwartz*, 2002] mainly built of pelagic sediments [*De Wever and Caby*, 1981; *Lemoine et al.*, 1984; *Polino*, 1984] scraped off the underlying oceanic crust during subduction.

2.2. Constraints From P-T-t Paths and Exhumation Rates: Distinct Exhumation Mechanisms for Oceanic Crust and Sediments?

[7] We compiled available P-T-t paths and estimated average exhumation rates for the oceanic units of the western Alps (Figure 1b). In this study, the continental P-T-t paths of Dora Maira and Gran Paradiso are shown only for comparison and briefly discussed. Despite contrasting P-T peaks, the maximum burial conditions of the various units line up along a typical HP-LT metamorphic thermal gradient of ~8°C km^{-1} (Figure 1c), which suggests that they underwent comparable thermal regimes. All of them were already largely exhumed to midcrustal depths of ~15–20 km at around 30–35 Ma, when collision developed.

[8] The average exhumation rates for the ocean-derived units are somewhat different, however, for the Schistes Lustrés and for the Monviso and Zermatt-Saas units (Figure 1b). For the SL complex, *Agard et al.* [2002] estimated the corresponding exhumation rates on the order of 1–2 mm yr^{-1} and demonstrated that contamination of the samples by excess argon was limited, because their radiometric ages are systematically consistent with the observed deformation chronology. Indeed, each of the three different deformation stages, D1, D2 and D3 ([*Agard et al.*, 2001]; whose pressure estimates are >15 kbar, 12–14 kbar, and 5–7 kbar respectively; Figure 2a), is associated with specific radiometric ages (Figure 2b). Between the D2 and D3 stages, the exhumation rate is well constrained at ~2.5 mm yr^{-1}. The larger scatter of the HP ages (D1; Figure 2b) may nevertheless be explained by small amounts of excess argon, as documented at HP conditions for several Alpine studies [e.g., *Arnaud and Kelley*, 1995; *Scaillet*, 1996; *Baxter et al.*, 2002; *Reddy et al.*, 2003]. Taking into account only the younger ages for D1 could raise the estimated exhumation rates to a maximum of 5 mm yr^{-1} for the first exhumation stage (Figure 2b). By comparison, higher exhumation rates were obtained for Monviso or Zermatt-Saas units, between ~1–4 [*Bowtell et al.*, 1994; *Inger et al.*, 1996], 5–10 [*Duchêne et al.*, 1997b; *Reinecke*, 1998] and 26 mm yr^{-1} [*Amato et al.*, 1999].

[9] This contrast among ocean-derived units is also apparent in the geological map (Figure 1a, inset). Indeed, blueschist facies sedimentary units with minor crustal lenses (such as the SL complex) dominate to the west, whereas large, mainly eclogitic oceanic crust bodies closely associated with serpentinites (such as Monviso and Zermatt-Saas) mainly crop out to the east [*Pognante*, 1991]. In addition, metamorphic P-T conditions evolve progressively in the former [*Agard et al.*, 2001; their Figures 5 and 7], whereas slices of units with contrasted P-T peaks characterize the latter [*Messiga et al.*, 1999; *Schwartz et al.*, 2000a]. The Monviso and Zermatt-Saas units are also closely associated in space with the continental Dora Maira and Gran Paradiso internal crystalline massifs (ICM, Figure 1a) and show similar exhumation-related tectonic patterns [e.g., *Philippot*, 1990; *Henry et al.*, 1993; *Van der Klauw et al.*, 1997]. The values of the exhumation rates for the UHP Dora Maira unit are still debated (Figure 1b), but the prevalent view considers

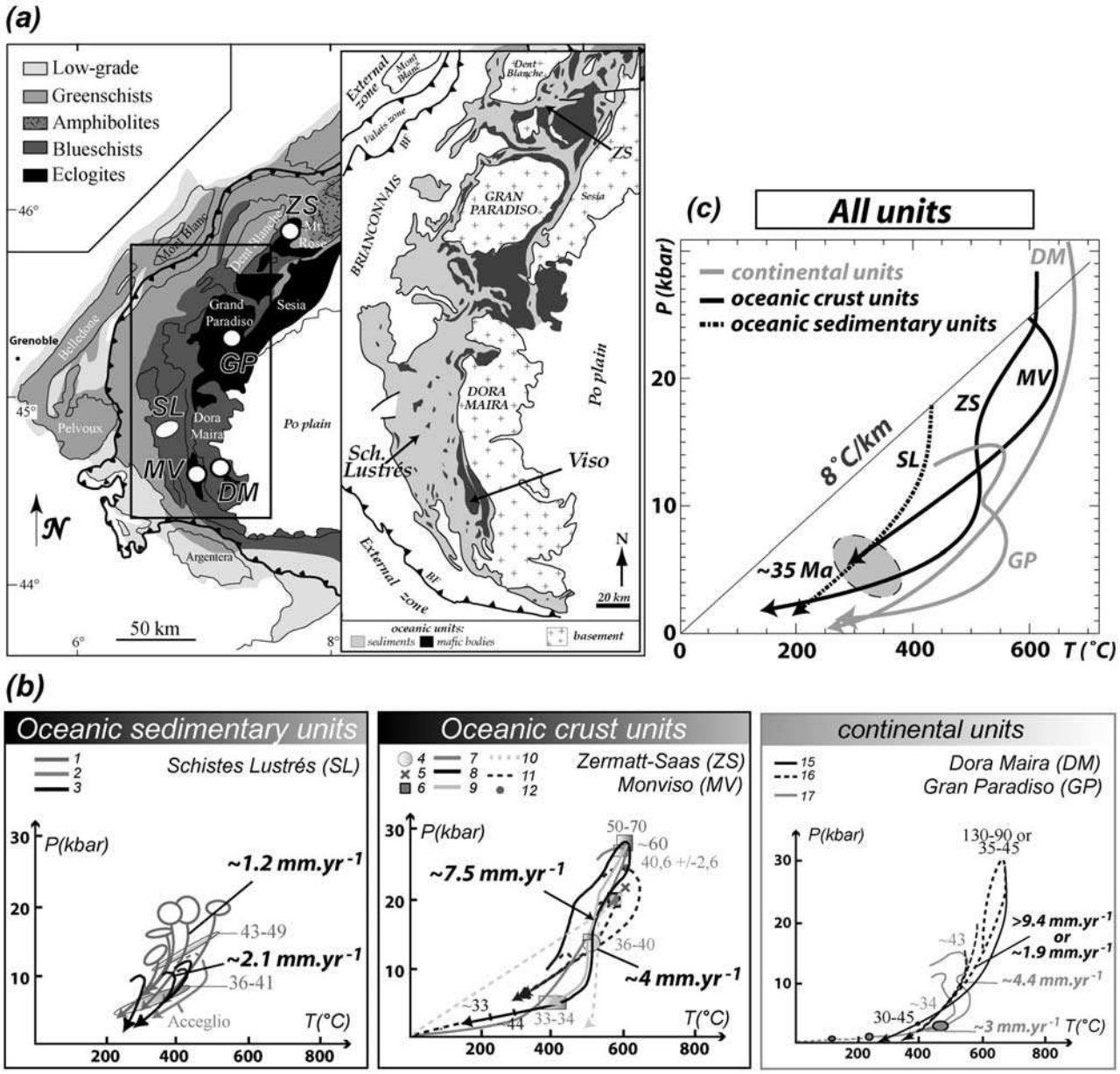

Figure 1. (a) Simplified metamorphic map [after *Frey et al.*, 1999] and location of the units where pressure-temperature-time (P-T-t) paths are taken from. (inset) Map presenting the repartition of the oceanic-derived units. (b) P-T-t paths for oceanic units (black boxes) for (SL) ''Schistes Lustrés'' unit, (ZS) Zermatt-Saas unit, and (MV) Monviso unit. P-T-t paths of continental units are given for comparison in gray box for (DM) Dora Maira and (GP) Gran Paradiso. Numbers refer to (1) [*Agard et al.*, 2001]; (2) [*Schwartz et al.*, 2000b]; (3) [*Schwartz et al.*, 2000a]; (4) [*Ernst and Dal Piaz*, 1978]; (5) [*Meyer*, 1983]; (6) [*Barnicoat and Fry*, 1986]; (7) [*Van der Klauw et al.*, 1997]; (8) [*Reinecke*, 1998]; (9) [*Amato et al.*, 1999]; (10) [*Widmer and Thompson*, 2001]); (11) [*Schwartz et al.*, 2000a]; (12) [*Cliff et al.*, 1998; *Messiga et al.*, 1999]; (15) [*Henry et al.*, 1993]; (16) [*Duchêne et al.*, 1997b]; and (17) [*Brouwer et al.*, 2002]; ages are consistent with *Hurford and Hunziker* [1989]. (c) Simplified P-T paths for the above units. Some of the P-T paths present a slight heating at about 35 Ma (e.g., Zermatt-Saas zone, Gran Paradiso) coeval with the medium-pressure medium-temperature Lepontine metamorphic overprint of the central Alps (5–7 kbar, 650–700°C; [e.g., *Todd and Engi*, 1997]), which presumably marked the inception of collisional processes [e.g., *Goffé et al.*, 2003].

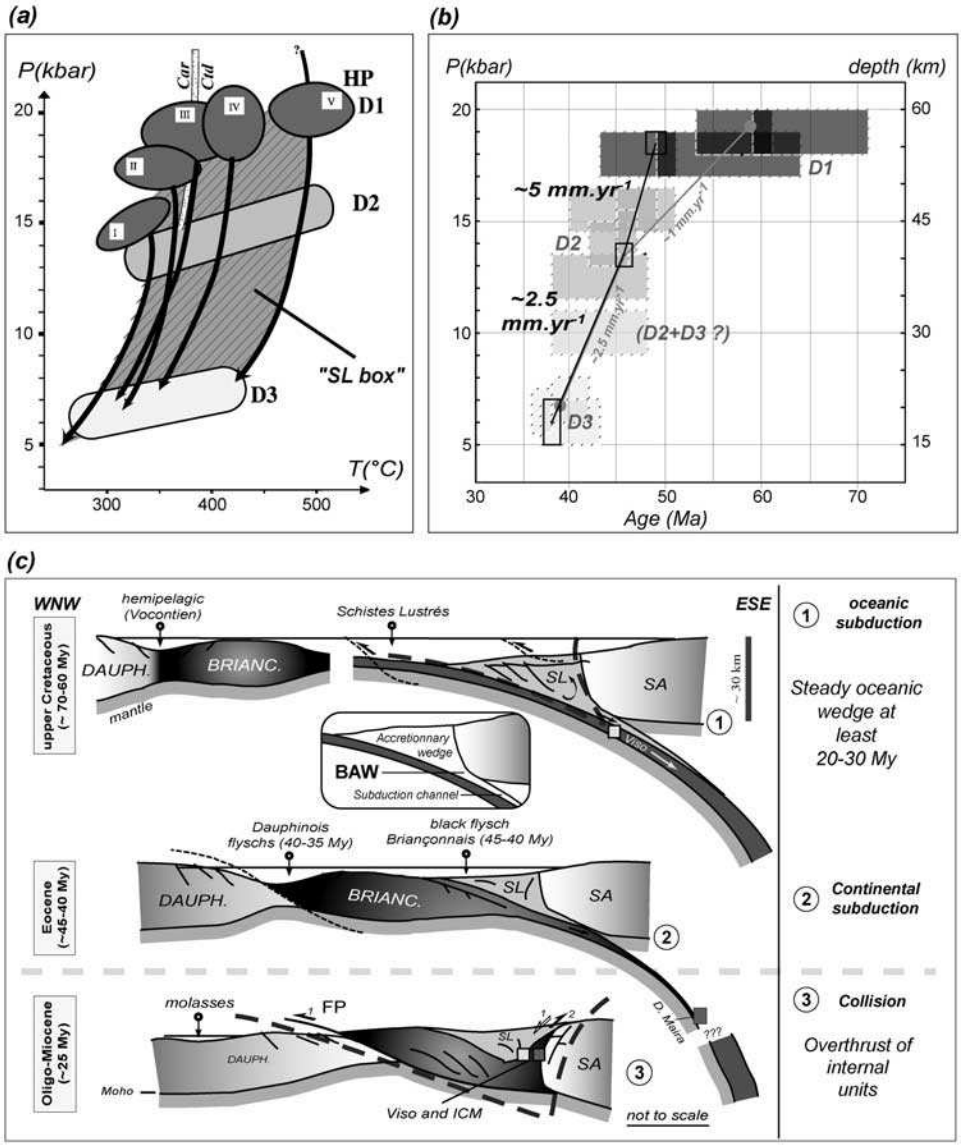

Figure 2. (a) P-T-deformation paths for various parts of the paleoaccretionary "Schistes Lustrés" (SL) complex (going eastward from I to V [after *Agard et al.*, 2001, 2002]). The "SL box" (shown also in Figure 9) corresponds to the P-T domain crossed by the SL paths. D1, D2, and D3 correspond to the main tectonic stages (see text for details). (b) Exhumation rates for the SL complex. Gray rectangles with dashed contours: Age and pressure data for individual samples from *Agard et al.* [2001, 2002] are represented with the associated error bars. Gray dots are averaged P-t conditions and exhumation rates inferred by *Agard et al.* [2002]. Black rectangles are new averaged P-t conditions for the main tectonic stages and inferred exhumation rates (in black), taking into account the possible presence of minor excess argon during the HP D1 stage. (c) Schematic geodynamic evolution of the western Alps showing the location and fate of the oceanic accretionary wedge through time [after *Agard and Lemoine*, 2005]. See text for details. Abbreviations are SA: south Alpine; BAW: Bottom of the accretionary wedge; BRIANC: Briançonnais; DAUPH: Dauphinois; FP: Penninic front; ICM: internal crystalline massifs; SL: Schistes Lustrés.

rates $\geq$1–5 cm yr^{-1} [e.g., *Duchêne et al.*, 1997b; *Gebauer et al.*, 1997; *Rubatto and Hermann*, 2001].

[10] The greater exhumation velocities, tighter P-T loops (Figure 1b) and the spatial association of Monviso and Zermatt-Saas with the ICM suggest that the exhumation of such large oceanic crust bodies was different from that of the metasedimentary SL complex and/or that exhumation occurred later, during the locking of continental subduction and the exhumation of the European margin.

3. Problematic Issues and Modeling Choices

[11] The Alpine stage of oceanic subduction and wedge accretion evolution is schematically set back within the frame

of the Liguro-Piemontese Ocean closure in Figure 2c. In order to match natural observations related to the Alpine oceanic subduction with our numerical models, some key points need to be recalled.

[12] During the oceanic subduction of the Liguro-Piemontese Ocean, most of the oceanic sedimentary units from the Schistes Lustrés complex were equilibrated at HP conditions (stage D1) of 15–20 kbar and 350–450°C

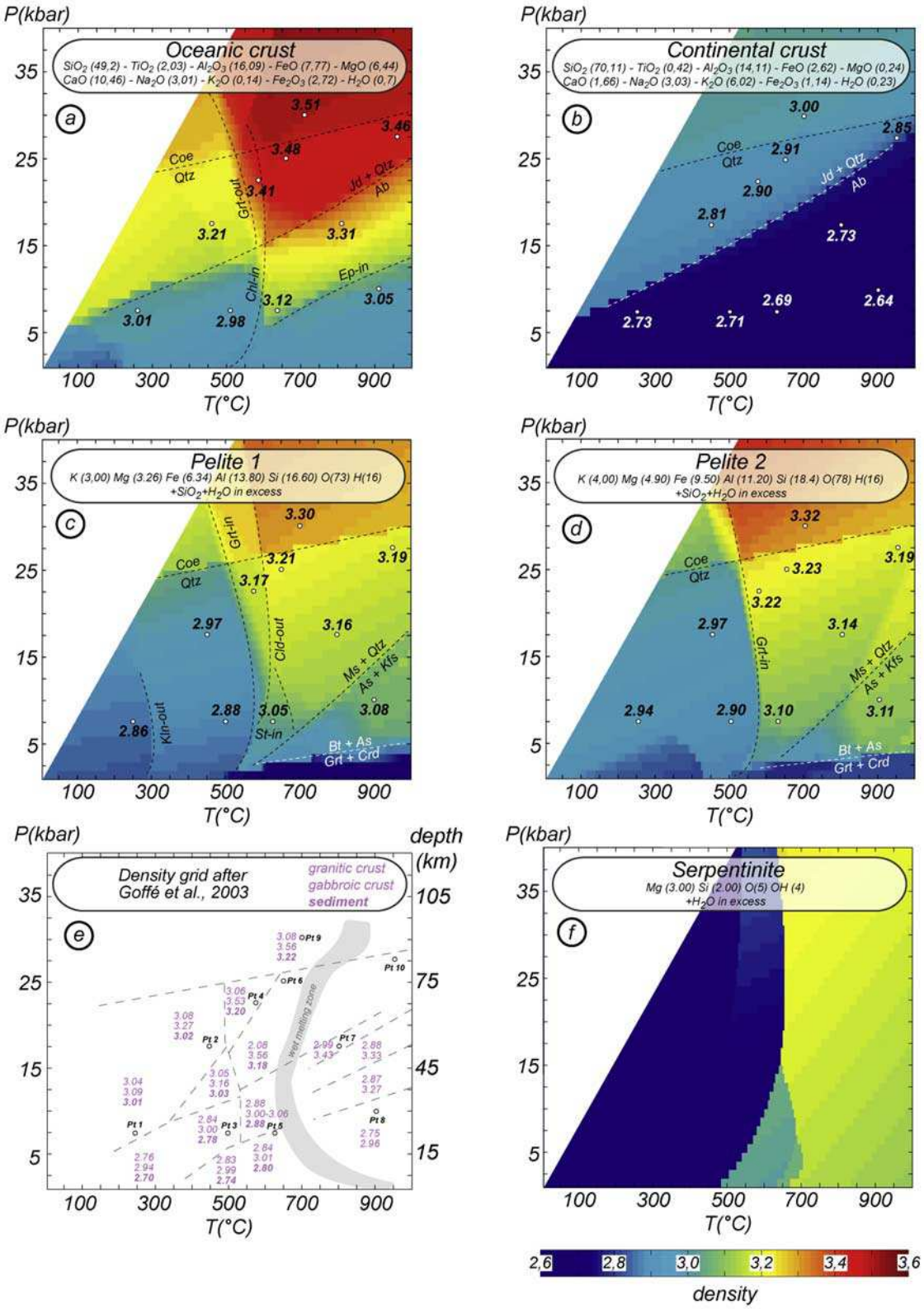

Figure 3

[*Agard et al.*, 2001] along a typical, cold thermal gradient of 8°C km^{-1} (Figure 2a). They were thus buried no deeper than the maximum depths of present-day accretionary wedges (<50 km) [e.g., *Brandon et al.*, 1998]. Radiometric dating suggests that these blueschists were exhumed during the oceanic convergence stage in steady state conditions during approximately 15 Ma at a rate of ~1–5 mm yr^{-1} (e.g., during the period between 60 and 45 Ma, Figure 2b). At the onset of collision, the exhumation rates were <1–2 mm yr^{-1} [*Agard et al.*, 2002].

[13] Petrological data inferred from oceanic crustal units yield the same P-T gradient (Figure 1c), yet the exhumation paths of these crustal units were different (Figure 1b). By contrast with the SL complex, Monviso and Zermatt-Saas crustal units were interleaved with serpentinites, were buried deeper into the subduction channel (below the bottom of the accretionary wedge; BAW, Figure 2c; [*Cloos*, 1982; *Cloos and Shreve*, 1988]) and brought back to the surface later (~45–40 Ma) and probably faster (>5 mm yr^{-1}).

[14] In order to better understand the mechanical and kinematic factors controlling the establishment of steady state accretionary wedges, we cannot use the earlier models of collisional orogens, which mostly prescribe wedge stability through kinematic assumptions. This is, for example, the case of the models based on the theory of plastic (brittle) critical wedge developed by [*Chapple*, 1978; *Davis et al.*, 1983; *Dahlen and Suppe*, 1988; *Dahlen*, 1990], which are not applicable at the scale of our problem, or the case of the models that use the "basal drag" or "S" point approach, which kinematically constrain the mantle and/or crustal part [e.g., *Beaumont et al.*, 1994; *Jamieson et al.*, 1998; *Willet*, 1999; *Beaumont et al.*, 2001; *Gerya et al.*, 2002; *Vanderhaeghe et al.*, 2003].

[15] The fully dynamic approach with unconstrained mantle part is clearly more appropriate [e.g., *Burov et al.*, 2001; *Pysklywec et al.*, 2002; *Gerya and Yuen*, 2003; *Gerya et al.*, 2004; *Toussaint et al.*, 2004; *Stöckhert and Gerya*, 2005]. It also allows for a greater choice of rheologies and lithospheric structures: Newtonian viscosity and Drucker-Prager plasticity and monolayered lithosphere [*Pysklywec et al.*, 2002], or nonlinear viscosity, Mohr-Coulomb plasticity and multilayer crust/lithosphere [*Burov et al.*, 1999; *Petrini and Podladchikov*, 2000; *Burov et al.*, 2001; *Toussaint et al.*, 2004; *Stöckhert and Gerya*, 2005], for example.

[16] In this study, we mainly follow the approach of *Toussaint et al.* [2004] by considering a multilayer lithospheric structure with a visco-elasto-plastic rheology. We combine this approach with that of *Gerya et al.* [2002, 2006] by introducing an additional thermodynamic module that allows for progressive density changes. We also use a dense passive marker array to trace particle trajectories, which allows us to obtain synthetic P-T-t paths.

4. Numerical Approach

[17] The governing equations and details of their numerical implementation are provided in Appendix A. The numerical code PARA(O)VOZ v7-9 (evolution of Paravoz v3 [*Poliakov et al.*, 1993]), used in this study, is based on the FLAC technique [*Cundall and Board*, 1988; *Cundall*, 1989] and allows to solve simultaneously Newtonian dynamic equations of motion (A1) and the heat transfer equation (A3) in a Lagrangian formulation. We assume that quasi-static approximation applies at geological strain rates, which allows us to use the inertial term in (A1) to lengthen the numerical time step. Adjustable viscous damping is then used to remove nonphysical elastic waves from the model [*Cundall*, 1989]. We also assume that the rock behavior is visco-elasto-plastic (A2, A5, A6). At each moment of time and location, the effective rheological behavior is determined by current strain rate, state of stress and temperature. Surface processes are accounted in the model using the common linear diffusion law (A7).

4.1. Implementation of Progressive Density Changes

[18] Buoyancy is an important component of force balance in subduction zones [*Bousquet et al.*, 1997; *Burov et al.*, 2001; *Doin and Henry*, 2001]. It is affected by density changes due to thermal expansion (A4) and metamorphic reactions. The system behavior is also sensitive to the rate of density changes. For this reason, the thermodynamic THERIAK algorithm [*De Capitani*, 1994] has been incorporated to account for progressive density changes instead of using a rough density grid based on metamorphic facies as in *Toussaint et al.* [2004]. THERIAK uses the JUN92.cc thermodynamic databases of *Berman* [1988] to minimize free Gibbs energy G and calculates (1) the stable mineral assemblage and (2) equilibrium phase compositions for a given chemical composition at specified P-T conditions [*De Capitani and Brown*, 1987]:

$$G = \sum_{i=1}^{n} \mu_i N_i \tag{1}$$

where μ_i is the chemical potential and N_i is the moles number for each component i constitutive of the assemblage.

[19] To save computation time, the density field is precomputed at the beginning of the computations for several typical bulk chemical compositions (Figure 3 and Appendix B). The P-T space is discretized over a fine regular grid with

Figure 3. Rock chemical compositions and densities used in PARA(O)VOZ for (a) oceanic crust, (b) continental crust, and (c–d) sediments. Densities were calculated with THERIAK [*De Capitani*, 1994]. The reactions responsible for large density variations (e.g., garnet- or coesite-forming reactions) are also shown. Density values refer to the mineral assemblages (see Appendix B) calculated at a given P-T with THERIAK to test the validity of our density grid. (Figure 3a) MORB basalt [after *Carmichael*, 1989]; (Figure 3b) granite [after *Carmichael*, 1989]; (Figure 3c) Pelite 1; (Figure 3d) Pelite 2 (see text for details about differences between them); (e) Density diagram after *Goffé et al.* [2003] shown for comparison; (f) Density field for serpentinite (used for the calculations of Figure 11). For the mantle, not shown here, the chemical composition of *Hofmann* [1988] was used.

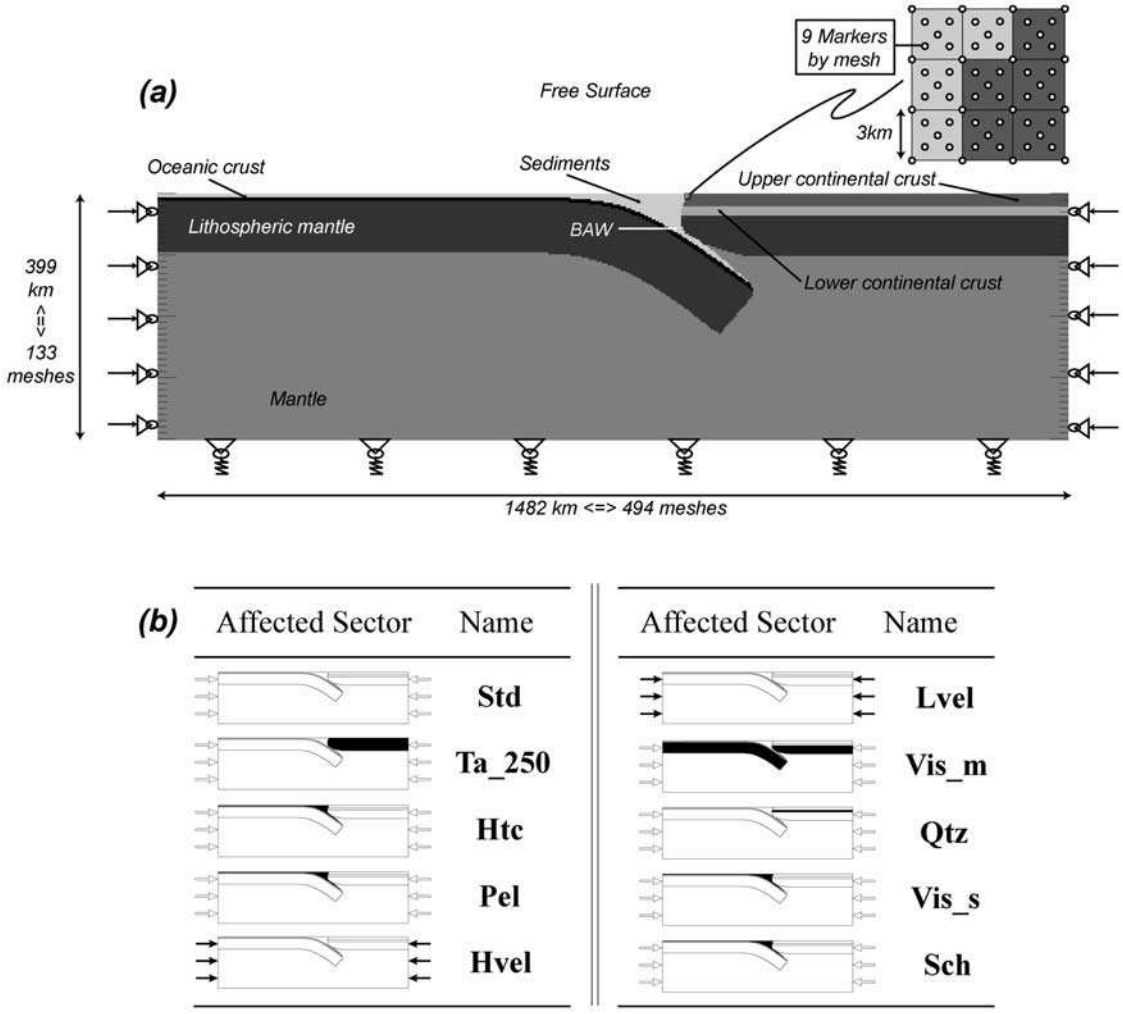

Figure 4. (a) Initial model setup for our oceanic subduction models (see text for details). BAW: Bottom of the accretionary wedge. (b) Name of the different numerical experiments (see Table 2) and localization of the affected part of the model with respect to the initial one.

interval of 100 MPa for pressure and 5°C for temperature. The mineralogical composition and hence density are reevaluated every 10^4 time steps (~200 ka) according to the current P-T conditions within PARA(O)VOZ. These new effective density values (ρ_{eff}) subsequently affect, during the experiment, both the mechanical equations ((A1) and (A4)) and the heat equation (A3). Equivalent stresses are applied to the elements to account for volume-density changes associated with the metamorphic transitions.

4.2. Tracking P-T-t Trajectories

[20] The compressible full stress formulation of PARA (O)VOZ allows the computation of P-T-t paths because the pressure is calculated as the trace of full stress tensor rather than on the base of common lithostatic assumptions (i.e., $P = \rho gz$). PARA(O)VOZ solves the governing equations ((A1) −(A7), see Appendix A) in Lagrangian framework (i.e., following the particle paths). However, geodynamic problems require modeling of both, very large strains and displacements. Hence to preserve the numerical accuracy, it is necessary to remesh the Lagrangian grid as soon as it becomes critically distorted. Remeshing of discrete parameter fields such as material phase numbers may induce artificial, nonphysical displacements of the material. To overcome this problem, a dense passive marker array (nine markers per element) was used to keep track of the material field, pressure and temperature with time, as a supplement to the main Lagrangian grid. For each mesh element (Figure 4a), four markers are placed at the nodes of each element, one at the barycenter of the element, and four others at the barycenters of the four subtriangles constituting the element. A total of 394840 markers are thus distributed within the model space. Within the Lagrangian finite volume mesh of PARA(O)VOZ, composed of quadrilateral elements subdivided onto overlapping pairs of triangle subelements, the computational cost of tracing particles is minimal because the trilinear shape functions of the triangular subgrid allow for fast detection of the element containing a particular marker and for interpolation of the corresponding grid values to the marker (see Appendix C).

[21] Interpolation of the parameter fields associated with the remeshing is a common source of numerical diffusion. This specifically applies to the interpolation of the discrete

Table 1. Rheological Parameters Used in All Experiments for Each Unit/Phase[a]

		Sediments						
		Quartz	Schists[b]	Oceanic Crust, Olivine	Continental Upper Crust, Quartz	Continental Lower Crust, Diabase	Lithospheric Mantle, Olivine	Asthenosphere Mantle, Olivine
Viscosity parameters	N	3	31	3	3	3.05	3	3
	A, $MPa^{-n}\ s^{-1}$	6.8×10^{-6}	1.3×10^{-67}	7×10^{3}	6.8×10^{-6}	6.3×10^{-2}	7×10^{3}	7×10^{3}
	E, J mol^{-1}	1.56×10^{5}	0.98×10^{5}	5.10×10^{5}	1.56×10^{5}	2.76×10^{5}	5.10×10^{5}	5.10×10^{5}
	References	R and M	S and K	G and E	R and M	C and T	G and E	G and E
Elastic parameters	λ, Pa	1×10^{10}		3×10^{10}	3×10^{10}	3×10^{10}	4×10^{10}	4×10^{10}
	μ, Pa	1×10^{10}		3×10^{10}	3×10^{10}	3×10^{10}	4×10^{10}	4×10^{10}
Cohesion, Pa		1×10^{6}		20×10^{6}	20×10^{6}	20×10^{6}	20×10^{6}	300×10^{10}
Frictional angle, °		5		10	15	30	30	2
k, $W\ m^{-1}\ K^{-1}$		2		3.5	2.5	2.5	3.5	3.5
χ, $m^2\ s^{-1}$		8.3×10^{-7}		8.75×10^{-7}	8.3×10^{-7}	6.7×10^{-7}	8.75×10^{-7}	8.75×10^{-7}
Density[c]		Pelite 2		oceanic crust	continental crust	continental crust	mantle	mantle
k_{eros}, $m^2\ yr^{-1}$		3000		3000	3000	3000	3000	3000

[a]Only one of these is changed at a time in each experiment (Table 2). References for viscosity parameters (n, A, and E) are from R and M [*Ranalli and Murphy*, 1987], S and K [*Shea and Kronenberg*, 1992], G and E [*Goetze and Evans*, 1979], and C and T [*Carter and Tsenn*, 1987]. Abbreviations are k: thermal conductivity; χ: thermal diffusivity; and k_{eros}: erosion coefficient. Thermal model used is also recalled: $T_s = 0°C$; $T_l = 1330°C$; $H_s = 9.5 \times 10^{-10}\ W\ kg^{-1}$; $h_r = 10$ km, with T_s: initial temperature at the top of the model; T_l: initial temperature at the base of the thermal lithosphere; H_s: surface heat production; and h_r: radiogenic decay depth.

[b]Parameter used only in exp. Sch.

[c]See Figure 3 for more details regarding density estimates.

parameter fields such as the numbers of material phases (the term ''phase'' identifies a particular material type and points to a set of rheological parameters, physical properties and a bulk chemical composition specific to this material (see Table 1)). To minimize the numerical diffusion, the initial material phase for each marker is stored in memory, starting from the initial calculation step. During remeshing, each new grid element receives the predominant phase of the markers found inside this element. A similar approach is used for other element quantities. During our experiments, about 70% of all markers were ''stable'', i.e., never changed their initial phase number.

[22] Because of the large number of passive markers (nine $\times$ number of elements), post processing becomes a computing issue. The strategy used here consists in (1) eliminating the ''unstable'' markers, (2) representing only one marker per element (preferably the central one), and (3) limiting the processing to the elements that were initially located in the area of interest (spanning between $300 \leq x \leq 1000$ km and $0 \leq z \leq 250$ km, Figure 5). This method is less sophisticated than that used by *Rudolph et al.* [2004] or *Gorczyk et al.* [2006] but is sufficient for our study.

5. Model Setup

5.1. Initial Geometry and Geotherm

[23] We aim at testing the evolution of an accretionary wedge resembling that of the Schistes Lustrés complex. For this reason, the initial geometry of the model corresponds to a supposed Alpine configuration at about 65 Ma. In all our experiments, a large ''model box'' 1500 km in height $\times$ 400 km in width (Figure 4a) with a spatial resolution of 3 $\times$ 3 km, is used in order to minimize boundary effects. We assume that oceanic subduction is already initialized with a dip of 35°. The use of this low value of dip is justified by the fact that no trace of back-arc extension is observed [e.g., *Heuret and Lallemand*, 2005] in the western Alps at this time [*Le Pichon et al.*, 1988; *Stampfli et al.*, 1998].

[24] For the input lithologies (Table 1), we use the flow properties of olivine to simulate both mantle and oceanic crust. The use of a single rheology for the mantle and the oceanic crust is justified by the fact that the oceanic crust is thin and composed of gabbros and basalts, whose flow properties are close to those of olivine [*Kohlstedt et al.*, 1995; *Mackwell et al.*, 1998]. Besides, since the major part of the oceanic crust remains brittle, its flow properties are of secondary importance. The continental crust and sediments are simulated using quartz rheology (= granites and granitoids). In addition, several experiments described in section 6.3 tested the effect of stronger lower crustal lithology (diabase) and of stronger or weaker sediments.

[25] In subduction zones, the downward translation of cold slab material produces complex thermal structures [*Royden*, 1993; *Davies*, 1999]. In our model, the input thermal structure relies on the conventional oceanic geotherm for the oceanic part (left side) of the model (Figure 5 and Table 1) considering a 100 km-thick lithosphere with a basal temperature of 1330°C. The continental part (right side) is based on the plate cooling model modified from *Parsons and Sclater* [1977] assuming a multilayer cooling half-space with thermal age of 160 Ma. This age accounts for the thermal rejuvenation due to the spreading of the Tethyan Ocean in the middle Jurassic [*Lemoine et al.*, 1986]. Radiogenic production in the continental crust and advection of radiogenic heat sources are also taken into account (see section 6.1).

5.2. Uncertainties of the Creep Laws and the Choice of Creep Parameters

[26] The main advantage of our explicit approach in terms of handling rheology lies in the fact that elasticity, plasticity and non-Newtonian viscosity are accounted for at minimum numerical cost (Appendix A). We can therefore interpret a posteriori the effective behavior of the modeled lithosphere instead of attributing a priori a simplified rheology to each of the tectonic units of the models, and avoid usual

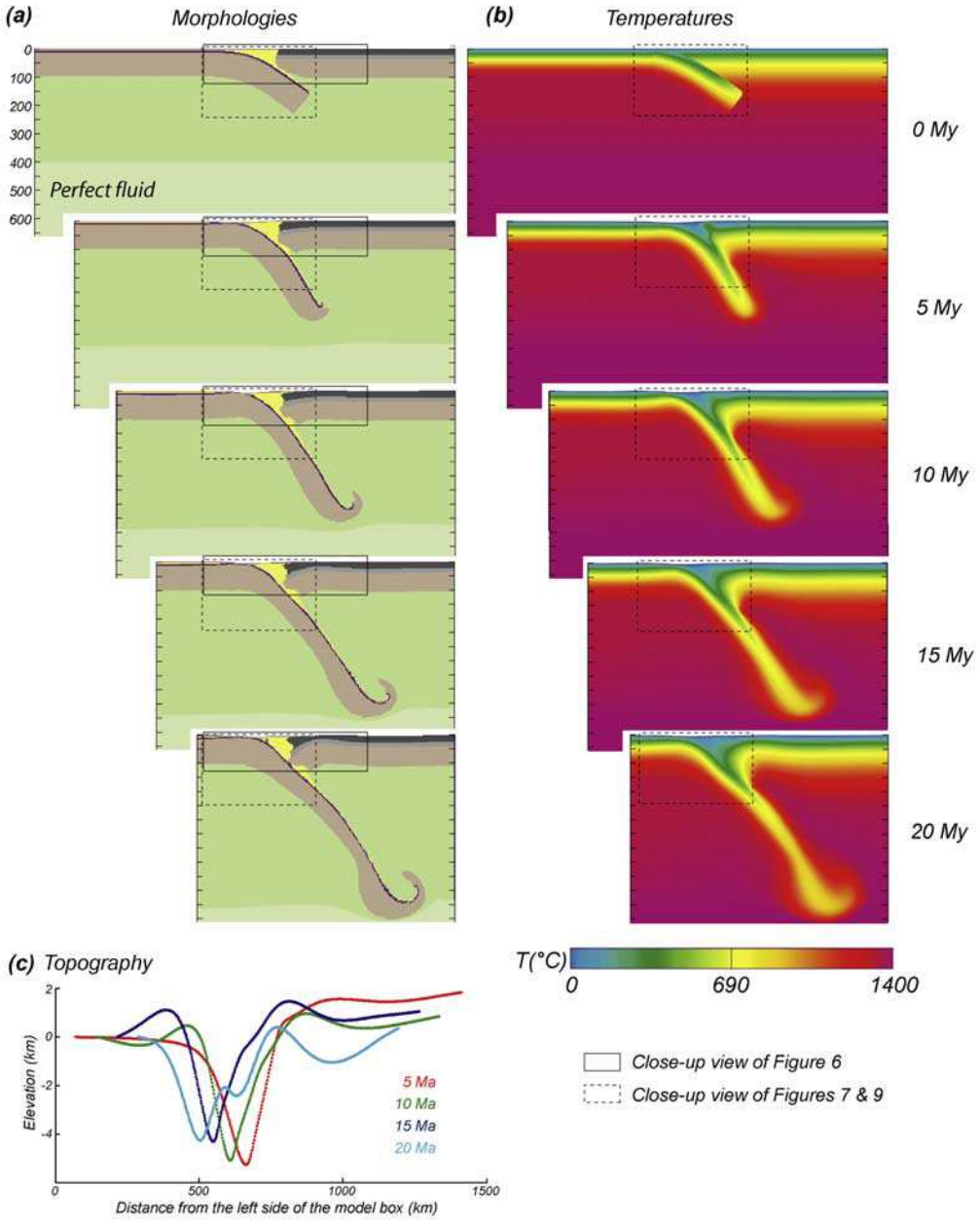

Figure 5. Morphology (a) and temperature (b) evolution of our subduction model during 20 Ma (*Std* experiment). Boxes: close-up views shown in Figures 6 (solid contours), 7, and 9 (dashed contours). (c) Evolution of the topography at 5–10–15–20 Ma.

simplifications such as neglecting elasticity, simplified failure criterions or fixed or only temperature-dependent viscosity.

[27] Besides, contrary to some common ideas, the choice of a visco-elasto-plastic rheology does not result in an increase of the number of variable rheological parameters. In the real lithosphere, the Poisson's ratio is constant (0.25), the Young modulus does not vary by more than one order of magnitude, and these values are commonly kept constant in elastic models of the lithosphere [e.g., *Turcotte and Schubert*, 2002]. The brittle plastic Byerlee's law [*Byerlee*, 1978] suggests a nearly invariable friction angle (30°–33°) for all crustal rocks, while cohesion values only differ for near-surface rocks. Consequently, the number of variable rheology parameters in our visco-elasto-plastic model is the same as in much simpler rheology models such as ductile viscous models.

[28] The only strongly varying and badly constrained rheological parameters of the model refer to the ductile creep flow [e.g., *Burov and Watts*, 2006]. Creep parameters A, n, H (Table 1, Appendix A, and equation (A6)) usually come from the "classical" rock mechanics studies [e.g., *Goetze and Evans*, 1979; *Carter and Tsenn*, 1987; *Ranalli and Murphy*, 1987; *Shea and Kronenberg*, 1992] or from

Table 2. List of the Experiments Performed[a]

Name	T_{age}	k_{sed}	Pelite Used	V	A_{lm}	Continental Lower Crust	A_{sed}	sed
Std	160	2	pelite1	3	A_{lm1}	diabase	A_{s1}	quartz
Ta_250	250	2	pelite1	3	A_{lm1}	diabase	A_{s1}	quartz
Htc	160	4	pelite1	3	A_{lm1}	diabase	A_{s1}	quartz
Pel	160	2	pelite2	3	A_{lm1}	diabase	A_{s1}	quartz
Hvel	160	2	pelite1	6	A_{lm1}	diabase	A_{s1}	quartz
Lvel	160	2	pelite1	1.5	A_{lm1}	diabase	A_{s1}	quartz
Vis_m	160	2	pelite1	3	A_{lm2}	diabase	A_{s1}	quartz
Qtz	160	2	pelite1	3	A_{lm1}	quartz	A_{s1}	quartz
Vis_s	160	2	pelite1	3	A_{lm1}	diabase	A_{s2}	quartz
Sch	160	2	pelite1	3	A_{lm1}	diabase	A_{s1}	schists

[a]Emphasis on the parameter tested is readily apparent in the name; see also Figure 4b. Abbreviations are T_{age}: thermal age for the continental lithosphere (Ma); and k_{sed}: thermal conductivity for the sediment material (W m^{-1} K^{-1}). A_{lm} is the preexponential factor for the viscosity of the lithospheric mantle (MPa^{-n} s^{-1}). The A_{lm1} value is 7.10^3 MPa^{-n} s^{-1} [*Goetze and Evans*, 1979]. The A_{lm2} value corresponds to the A_{lm1} value divided by 10. A_{sed} is the preexponential factor for the viscosity of the sedimentary material (MPa^{-n} s^{-1}). The A_{s1} value is $6{,}8.10^{-6}$ MPa^{-n} s^{-1} [*Ranalli and Murphy*, 1987]. The A_{s2} value corresponds to the A_{s1} value multiplied by 10. Continental lower crust is the material used in order to simulate the continental lower crust. V is the convergence rate (cm yr^{-1}), i.e., the total velocity of convergence applied at the boundaries of the models.

more specific studies that take into account the effects of fluid content, pressure and/or water fugacity [e.g., *Karato et al.*, 1986; *Karato*, 1998; *Mackwell et al.*, 1998]. *Kohlstedt et al.* [1995] and *Burov and Watts* [2006] pointed out, however, that despite the recent improvement of internal precision of rock mechanics data, no progress was made in reducing the uncertainties of their application, either to simplest bimineral aggregates or to geological time and space scales. Owing to the lack of significant difference between the new and old data for leading lithospheric lithologies [*Burov and Watts*, 2006], specifically if one takes into account the huge scatter due to the unknown fluid content and mineralogical composition, we have chosen to ''stick'' to the ''classical'' data sets.

[29] In the deep mantle domain, we use large values of cohesion for the mantle and asthenosphere (see Table 1) in order to force these visco-elasto-plastic materials to behave visco-elastically (or, in fact, viscously, if one takes into account small Maxwell relaxation times at such depths) without changing the basic visco-elasto-plastic constitutive model. Switching-off plasticity in the deep mantle is not compulsory but avoids ''fake'' brittle localization at great depths since it is known that Mohr-Coulomb or Drucker-Prager plasticity is not applicable for rocks at large confining pressures [e.g., *Ranalli*, 1995].

[30] The use of olivine instead of diabase for the oceanic crust is justified by the fact that their ductile strengths fields are largely overlapping [*Mackwell et al.*, 1998], and that a large part of the oceanic crust remains near the surface and deforms in the brittle regime, which is independent of rock type.

5.3. Boundary Conditions and Assumptions

[31] In our model, we reproduce the boundary conditions used in most analogue models (Figure 4a), except that we account for surface processes (the upper boundary condition is a free surface exposed to erosion and sedimentation). The surface processes are modeled using the linear diffusion equation (A7) (Appendix A) with an erosion coefficient of 3000 m^2 yr^{-1} derived for corresponding settings in *Avouac and Burov* [1996].

[32] In order to avoid artificial prescription of internal evolution, particularly within the accretion wedge, depth-invariable velocity boundary conditions (2×0.75 to 2×3 cm yr^{-1}) were applied on the lateral sides of the model, in the same way as a moving rigid wall is used in analogue models [e.g., *Chemenda et al.*, 1995]. The alternative choice would be to apply boundary forces or velocity to the lithosphere alone, yet this would imply neglecting plate parallel mantle convection or mantle down-flow in subduction zones, or the influence of the deep mantle drag. This would also require prescribing the degree of plate-mantle coupling, which is a largely unknown parameter.

[33] The lower boundary condition corresponds to Winkler's basement with a low-density contrast (10 kg m^{-3}) and replaces the unmodeled deep mantle. The model is thus considered to overly an infinite space filled with a perfect fluid. When shortening occurs, the effect of the downward movement of the Winkler's basement is similar to that of the uprise of the mean surface in some analogue models, or of the outflow of the ''excessive asthenosphere'' through specially made holes in some others. The experiments were stopped when the lithosphere reached the 650 km depth, to avoid dealing with the upper-lower mantle phase transitions.

[34] We are aware of the fact that there is so far no ideal, or geologically plausible and physically consistent, model of the collision-subduction processes. We feel, however, that the application of shortening or basal shear to the lithosphere only, or the introduction of a specific S-point forcing the subduction [e.g., *Beaumont et al.*, 1999, *Pfiffner et al.*, 2000], would produce more errors than our choice. This choice is also compatible with previous analogue and many numerical models.

6. Fixed and Variable Parameters

[35] The initial geometry of the model (Figure 4a) did not change from one experiment to another. The influences of parameters such as subduction dip, oceanic geotherm or erosion rate have not been tested in this study. Nine other parameters such as initial age, density or rheology (Figure 4b and Table 2) were modified one by one in order to study their influence on the accretionary processes.

6.1. Thermal Properties for the Ocean and Sediments

[36] As mentioned in section 5.1, the thermotectonic age of 160 Ma accounts for thermal rejuvenation due to spreading of the Tethyan Ocean in the middle Jurassic [*Lemoine et al.*, 1986]. However, if one suggests that the degree of rejuvenation was less important, then the initial geotherm could rather correspond to the initial (Permian) age of the continental plate, i.e., ~250 Ma. For this reason, we tested the influence of both end member thermal ages for the continental plate (Jurassic and Permian). The age of 160 Ma (Figure 5) was used for the *Std* simulation and the age of 250 Ma has been used for the *Ta*_250 experiment.

[37] The thermal conductivity of sedimentary materials was another variable parameter. In nature, it fluctuates from

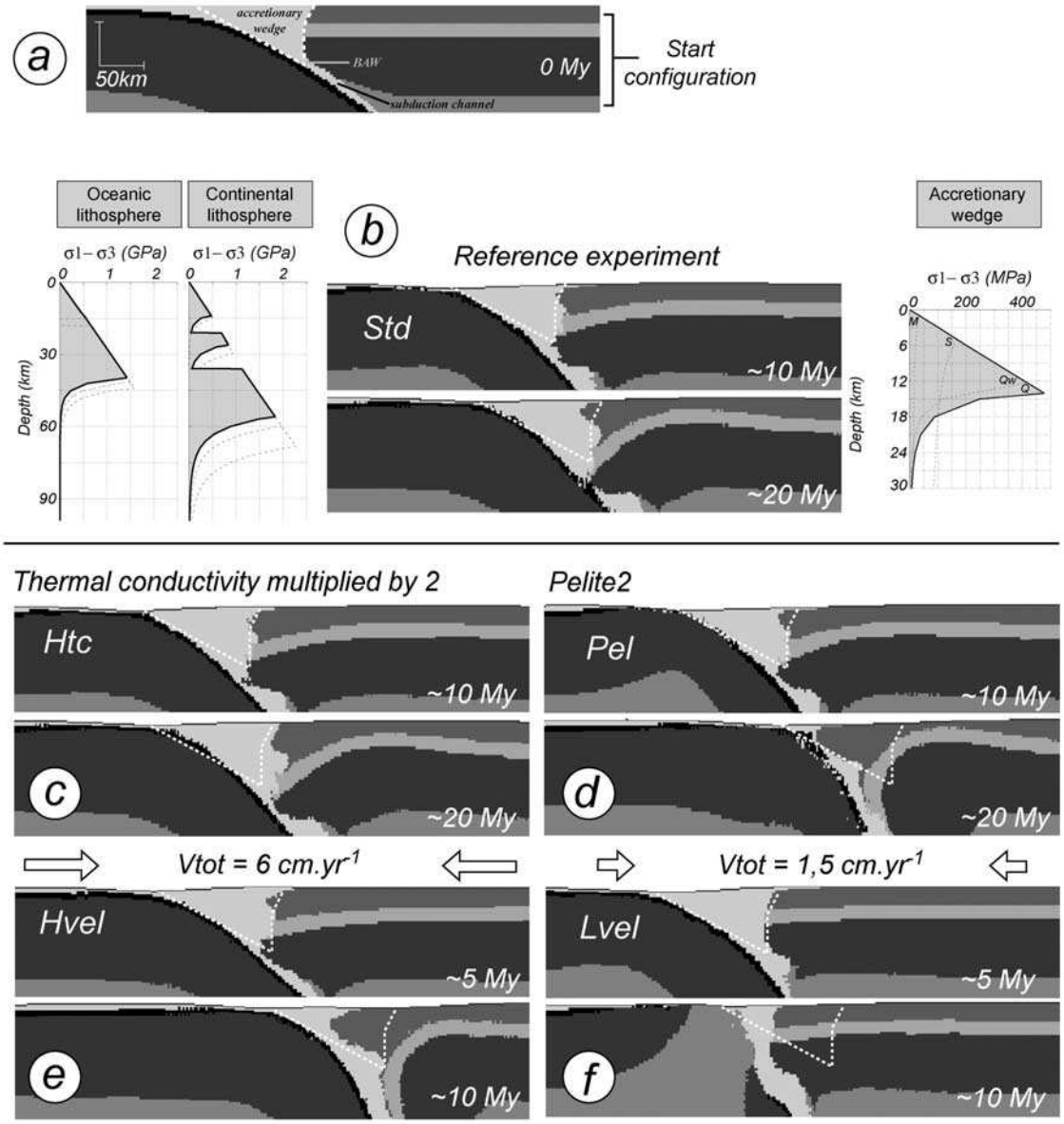

Figure 6. Close-up views showing the evolution of the accretionary wedge stability during the first 20 Ma for all experiments (location in Figure 5 for *Std* experiment). Pictures are taken at 10 and 20 Ma (except for the experiments "Lvel" and "Hvel", which stopped after 10 Ma, shown at 5–10 Ma). Gray coloring for phases is as for Figure 4. The right side box is cut at 300 km of the real right side box of the model (Figure 5). Start configuration is recalled at the top. For each experiment presenting a new rheological property (exp. Ta_250, Vis_m, Vis_s, Qtz, Sch), yield strength envelopes are traced for oceanic lithosphere, continental lithosphere, and for the accretionary wedge (S: schists; Qw: weak quartz corresponding to the exp. Vis_s; Q: quartz corresponding to the exp. *Std*). For the sake of comparison a white dotted triangle outlines the initial morphology of the accretionary wedge. See text for details.

1 to 5 W m^{-1} K^{-1} with low values for shales and sandstones (~1.2–4.2 W m^{-1} K^{-1}) and slightly higher values for limestones and dolomites (2–5 W m^{-1} K^{-1}) [*Turcotte and Schubert*, 2002]. The value used in standard (*Std*) simulation was 2 W m^{-1} K^{-1}, and a twice higher value was also tested in the high thermal conductivity (*Htc*) experiment.

[38] The internal heat production (Appendix A) of crustal rocks is computed assuming common exponential distribution with depth, with the decay length, h_r, of 10 km and surface heat production, H_s, of 9.5 × 10^{-10} W kg^{-1} [e.g., *Turcotte and Schubert*, 2002]. THERIAK computes the equilibrium densities of the rocks for given P-T conditions. For the experiments without THERIAK, thermal expansion, α, was set to the representative mean value of 3.1 × 10^{-5} K^{-1} [*Turcotte and Schubert*, 2002]. For computation of the initial geotherms, we also used commonly referred values of thermal diffusivity (Table 1): χ_{c1} = 8.3 × 10^{-7} m^2 s^{-1} for the upper crust and sediments; χ_{c2} = 6.7 ×

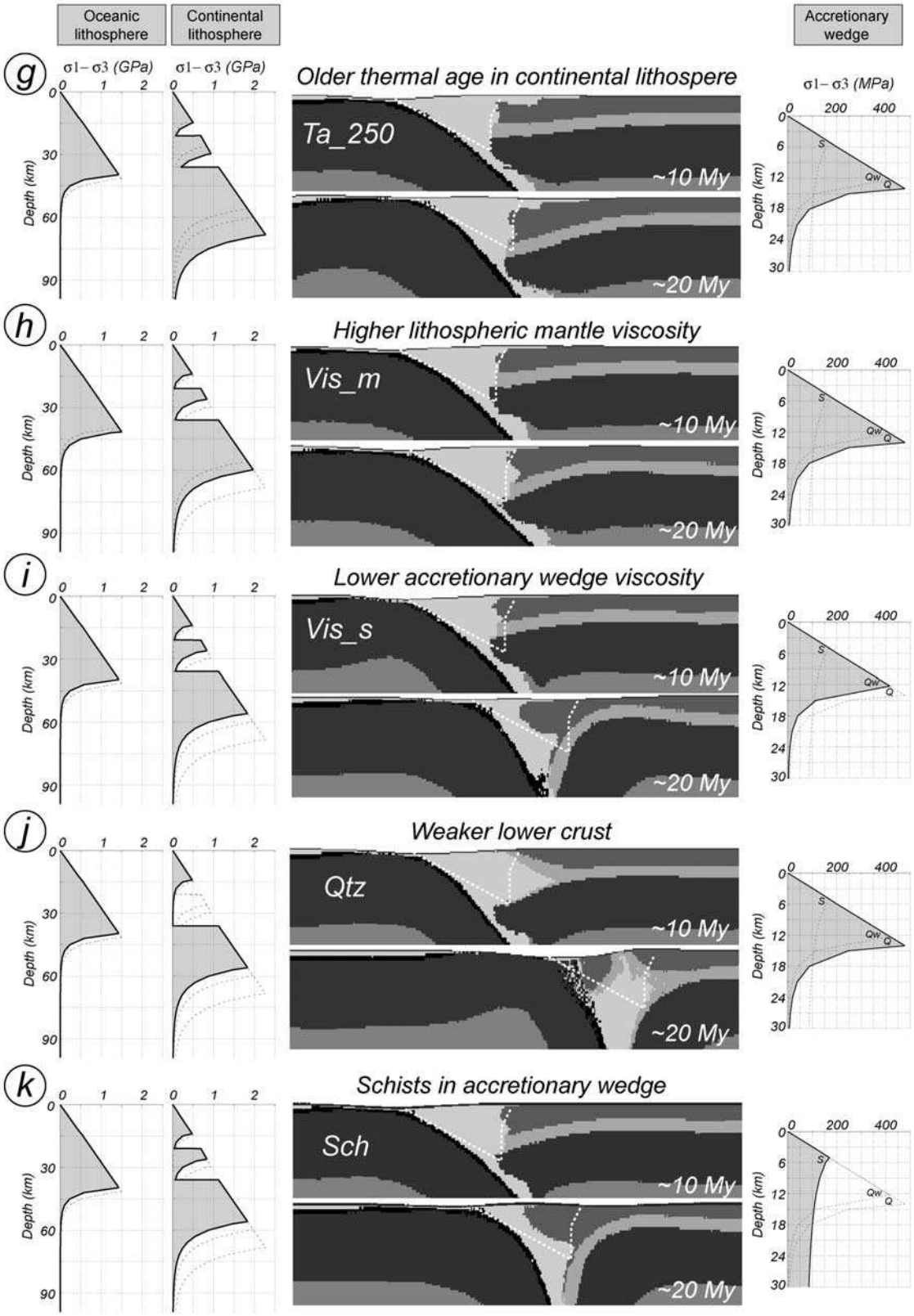

Figure 6. (continued)

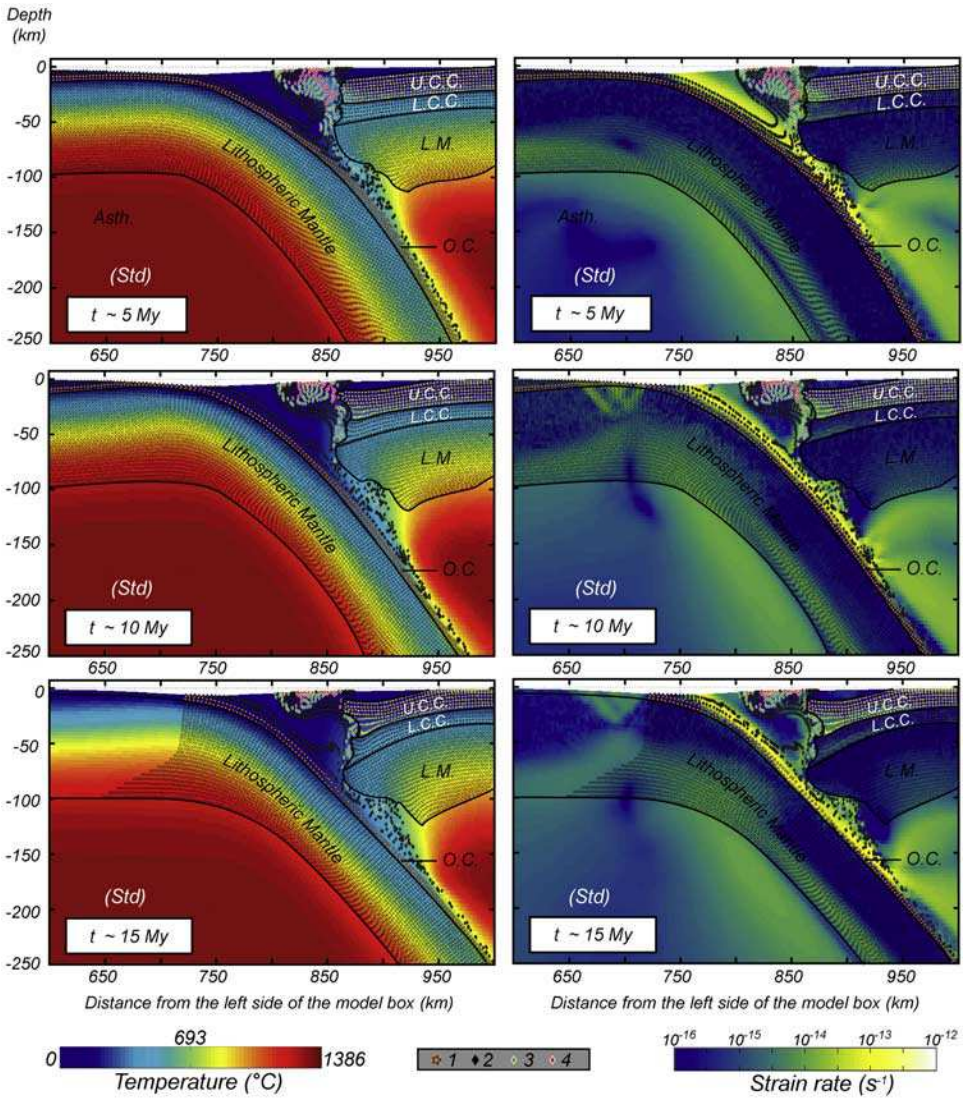

Figure 7. Close-up views focusing on the subduction channel at 5, 10, and 15 Ma. The evolution of markers on the geotherm (left) and on the strain rate (right) are presented for the *Std* simulation. Different shapes and color of markers correspond to (1) oceanic crust (O.C.); (2) sedimentary particles; (3) sedimentary particles passing through the Schistes Lustrés conditions (SL box, Figure 2a); (4) sedimentary particles crossing the SL box and exhumed to the surface; (5) upper continental crust (U.C.C.); (6) lower continental crust (L.C.C.); (7) lithospheric mantle (L.M.). Markers displacements within the accretionary wedge are described in Figure 8. Markers at the bottom of the accretionary wedge, located just at the top of the oceanic crust, are buried at depth in the subduction channel where the major part of the strain occurs. These particles never come back to the surface. The strain rate is also high where particles are being exhumed. In the middle of the wedge, strain rates are lower and coincide with a lower rotation velocity of particles.

10^{-7} m^2 s^{-1} for the lower crust; $\chi_m = 8.75 \times 10^{-7}$ m^2 s^{-1} for the mantle [e.g., *Turcotte and Schubert*, 2002].

6.2. Density of Sediments

[39] Densities for all material phases were computed using the THERIAK code (Figure 3) [*De Capitani*, 1994]. In order to test the influence of sedimentary density and bulk composition on the behavior of the accretionary wedge, two different pelitic assemblages were considered [e.g., *Spear*, 1993]. Aluminium-rich pelite 1 corresponds to a simplified assemblage made of 3 phengite + 1 garnet + 1 chlorite + 1 chloritoid and is used in the *Std* simulation. Pelite 1 shows a density evolution indistinguishable from the one calculated for the pelite of *Bücher and Frey* [1994]. Aluminium-poor pelite 2 is made of 2 phengite + 1 garnet + 1 chlorite + 2 biotite and is slightly denser than pelite 1 (Figure 3). Pelite 2 was used in the "*Pel*" simulation. These two pelites show values comparable to previous density estimates (Figure 3e) for natural pelites [e.g., *Goffé et al.*, 2003].

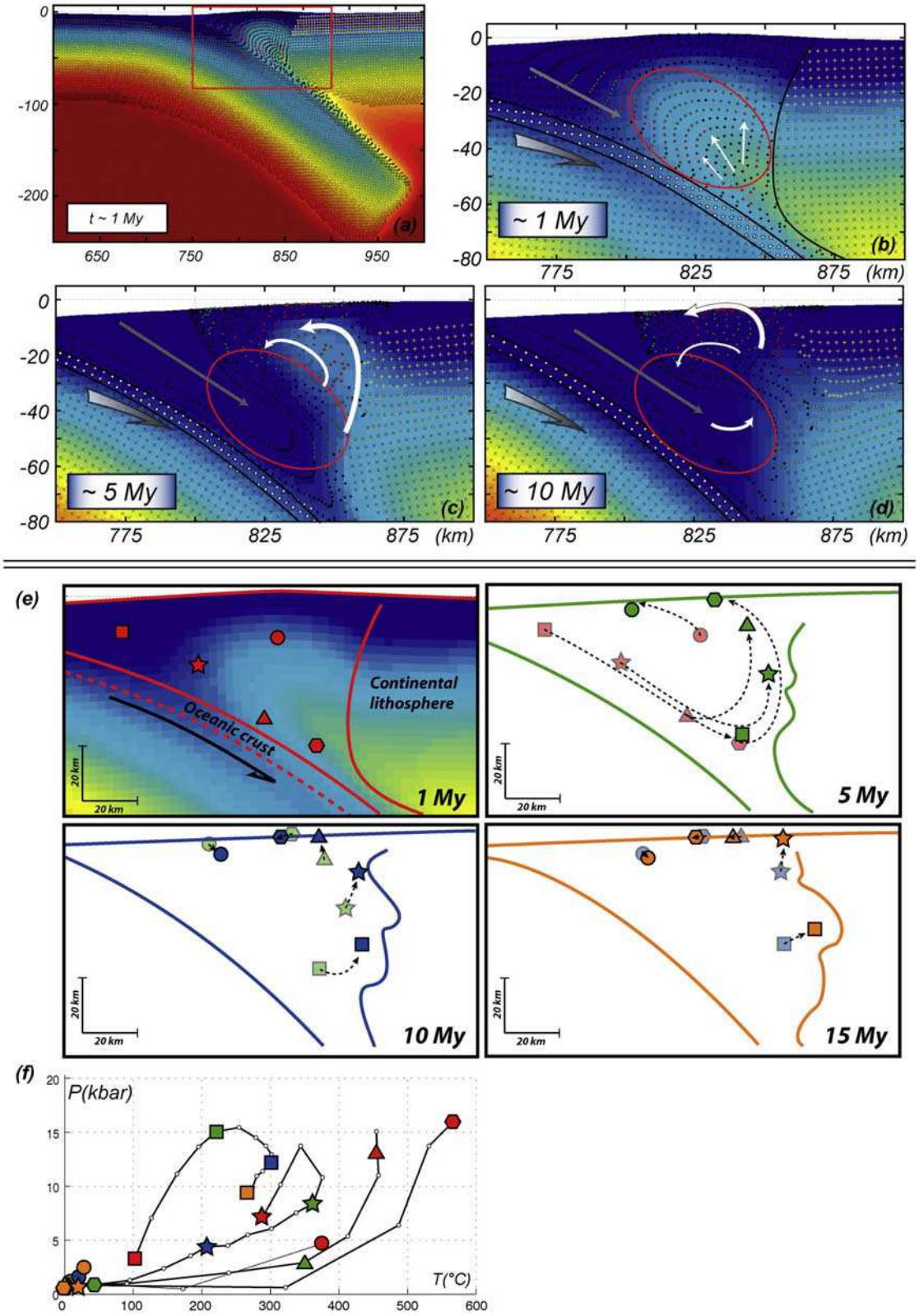
0
-100
-200
t ~ 1 My
(a)
650
750
850
950
0
-20
-40
-60
-80
~ 1 My
(b)
775
825
875
(km)
~ 5 My
(c)
~ 10 My
(d)
(e)
Continental lithosphere
Oceanic crust
20 km
1 My
5 My
10 My
15 My
(f)
P(kbar)
T(°C)
0
5
10
15
20
100
200
300
400
500
600

Figure 8

6.3. Rheological Parameters

[40] The effective rock viscosity η_{eff} (A6) depends on the strain rate, stress, temperature and rheological parameters (n, A and H) that were assigned according to the mineralogical composition and the assumed fluid content of the phase. As the fluid content is only implicitly included in the ductile creep parameters, we tested its influence by varying the preexponential parameter A. Hence in the experiment *Vis_m*, which explores a stronger lithosphere configuration, A of the lithospheric mantle was reduced by a factor of 10. In order to test the influence of the sediment viscosity on the behavior of the accretionary wedge, the parameter A (A6) was multiplied by a factor of 10 in the experiment *Vis_s*. Another weak material (Table 1), with rheological parameters of schist [*Shea and Kronenberg*, 1992] has also been tested (Exp. *Sch*).

[41] Several authors have recently suggested that at least a part of the lower crust may deform in brittle regime [*Déverchère et al.*, 2001; *Jackson*, 2002]. For this reason, model sensitivity to variations in the lower crustal strength has been also addressed by running and comparing two additional experiments. In the first experiment, quartz flow law parameters were inferred for the lower crust (exp. *Qtz*). In the second experiment (exp. *Std*), the lower crust had diabase flow law parameters. Figure 6 shows yield strength envelopes of oceanic lithosphere, continental lithosphere, and accretionary wedge for each set of experiments.

6.4. Convergence Rates

[42] Convergence rates inferred for the western Alps vary between 1 and 2 cm yr^{-1}. However, in most oceanic subduction zones worldwide, convergence rates are higher ($\sim$4–15 cm yr^{-1}; e.g., 4–5 cm yr^{-1} for the Cascades subduction zone on average since the Cretaceous [*Engebretson et al.*, 1985]). Consequently, in order to account for possibly higher initial convergence rates in the Alps, we tested three values of the convergence rate: moderate (3 cm yr^{-1} for the *Std* simulation), high (6 cm yr^{-1} for the experiment *Hvel*), and low (1.5 cm yr^{-1} for the experiment *Lvel*).

7. Results

[43] In all experiments, the convergence is mainly accommodated in the simple shear mode through subduction of the oceanic lithosphere, and the continental lithosphere only moderately deforms in the pure shear and bending/folding modes (Figure 5). The oceanic sediments circulate within the accretionary wedge (Figures 7 and 8), whereas the oceanic crust and mantle never return to the surface after burial. The presence of a free surface at the top of the model permits us to follow the evolution of topography due to erosion and sedimentation. In all experiments, the difference between the elevation of the subduction trench and the continental topography never exceeded 7 km as shown in Figure 5c for the *Std* experiment. The maximal above-sea level topography was $\sim$3–4 km, which is in agreement with present-day subduction zones.

7.1. Reference Experiment

[44] The large-scale evolution predicted within a representative reference experiment is shown in Figure 5. We briefly report here several observations that are useful for further comparison with other experiments. In this standard experiment, the accretionary wedge and thermal structure remained steady for at least 20 Ma (we call a wedge "stable" if its geometry does not significantly deviate from its initial shape; see dashed white lines on Figure 6). Strain is well localized along the subduction channel (Figure 7). Once the incoming particles reach depths >40–45 km (Figure 8), they are forced back to the surface, whereas the units buried at lesser depths tend to circulate within the accretionary wedge. Exhumation P-T-t paths predicted for the metasediments within the accretionary wedge (Figure 9) appear to be close to the natural ones (from $\sim$15–20 kbar and 350–400°C to the surface). Exhumation rates <4 mm yr^{-1} after 5 Ma are also in agreement with natural data (Figure 2b).

7.2. Evolution of the Accretionary Wedge Morphologies

[45] The effects of the different tested parameters are presented with respect to the reference experiment *Std* (Figure 5). To compare morphological structures of the wedge obtained in different experiments, we measure their "ability" to preserve their original shape. In all experiments that reproduce a stable wedge evolution, the characteristic time for a sedimentary particle to travel from the surface to the bottom of the wedge is on the order of 10 to 15 Ma (Figures 7 and 8).

7.2.1. Influence of the Thermal Age and Mantle Rheology

[46] The morphological evolution of the wedge for experiments *Ta_*250 (continental thermal age of 250 Ma), *Vis_m* (material parameter A of the lithospheric mantle reduced by a factor of 10) and *Htc* (thermal conductivity in sediments multiplied by a factor of 2) is similar to *Std*. The experiments show that the variation of the thermal age from 160 to 250 Ma, or an increase of the lithospheric mantle viscosity by a factor of 10, or the presence of twice more conductive sediments, have little influence on the morphology and stability of the wedge. The similar evolution of models *Ta_*250 and *Vis_m* results from the fact that

Figure 8. Spatial evolution of accretionary wedge markers (location box in (a)) for the *Std* experiment at 1, 5, and 10 Ma (b–d). Symbols are as for Figure 7. As early as 1 Ma (Figure 8b), the deflection of the marker grid shows two types of motion; part of the material is buried at depth and never returns to the surface, while particles initially lying at the bottom of the wedge (red ellipse) come back to the surface in 10 Ma (green and red circles). New sediment inputs (meshes without markers) are buried at depth. This burial of new material (gray arrow) is well delimited by the marker line corresponding to the initial model box surface. It reaches the corner zone where the first markers were exhumed from Figure 8b at 10 Ma (Figure 8d). (e) Tracking of five particles through time within the accretionary wedge and (f) associated P-T-t path. Colors in Figures 8e and 8f correspond to the time (red: 1 Ma; green: 5 Ma; blue: 10 Ma; orange: 15 Ma).

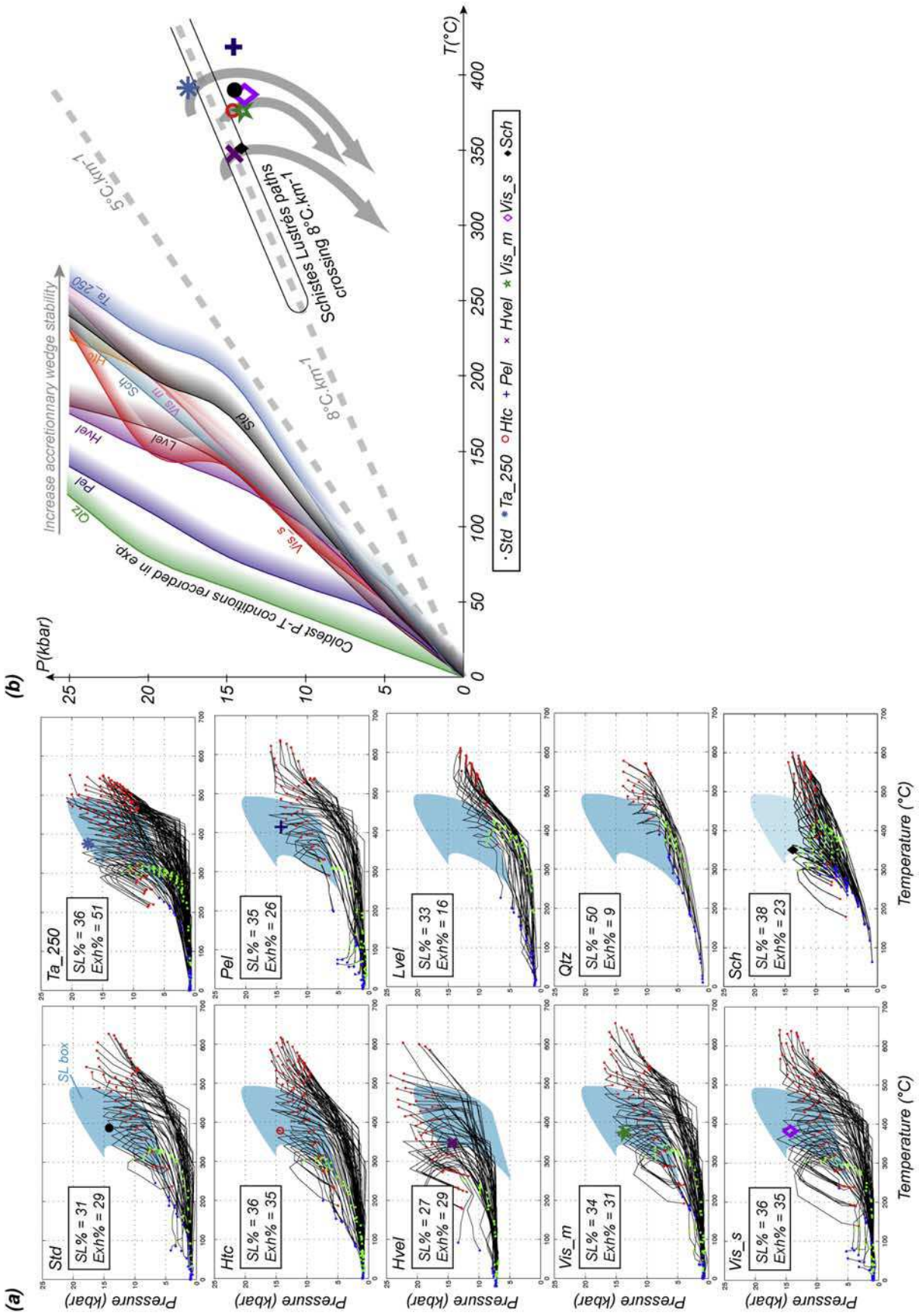
(a)
Std
SL% = 31
Exh% = 29
SL box
Ta_250
SL% = 36
Exh% = 51
Htc
SL% = 36
Exh% = 35
Pel
SL% = 35
Exh% = 26
Hvel
SL% = 27
Exh% = 29
Lvel
SL% = 33
Exh% = 16
Vis_m
SL% = 34
Exh% = 31
Qtz
SL% = 50
Exh% = 9
Vis_s
SL% = 36
Exh% = 35
Sch
SL% = 38
Exh% = 23
Pressure (kbar)
Temperature (°C)
(b)
P(kbar)
T(°C)
Increase accretionnary wedge stability
Coldest P-T conditions recorded in exp.
Qtz
Pel
Hvel
Lvel
Vis_s
Std
Vis_m
Sch
Htc
Ta_250
5°C.km-1
8°C.km-1
Schistes Lustrés paths
crossing 8°C.km-1
·Std •Ta_250 ○Htc +Pel ×Hvel ★Vis_m ◇Vis_s ♦Sch

Figure 9

increasing the thermal age leads to a colder mantle geotherm and consequently to a more viscous lithospheric mantle.

7.2.2. Influence of Crustal Rheology

[47] A weak lower continental crust (exp. *Qtz*) has a crucial effect on the stability of the accretionary wedge because this induces a decoupling zone between the upper crust and mantle lithosphere. The accreted sedimentary material in the wedge cannot be pressed upward along the soft hanging wall of the wedge and remains largely at depth (Figure 6j).

7.2.3. Influence of the Convergence Rate

[48] The experiments show that a high convergence rate (6 cm yr^{-1}) induces resorption of the accretionary wedge from 10 Ma onward (Figure 6e, exp. *Hvel*). Yet, a too low convergence rate (1.5 cm yr^{-1}) prevents continued subduction for a period longer than 10 Ma and the accretionary wedge cannot be preserved in this case (Figure 6f, exp. *Lvel*). The system is most stable at intermediate convergence rates on the order of 3 cm yr^{-1} (Figure 6b, exp. *Std*).

7.2.4. Influence of the Mineralogical Composition

[49] The experiments suggest that a dense, aluminium-poor pelite (Figure 3) prohibits formation of a stable accretionary wedge (Figure 6d, exp. *Pel*). In this experiment, most of these dense sediments are buried at depth and the size of the accretionary wedge decreases rapidly. A similar resorption phenomenon occurs when the viscosity of sediments is decreased by a factor of 10 (Figure 6i, exp. *Vis_s*). Hence low-density and/or high-viscosity sediments enhance the accretionary wedge stability.

7.3. Computed P-T-t Paths and Exhumation Rates

[50] The analysis of synthetic P-T-t paths obtained from the markers placed in the accretionary wedge (Figure 9a) permits to evaluate the compatibility of the models with petrology data. In steady wedge experiments (*Std*, *Ta_*250, *Htc* and *Vis_m*), more than 30% of the sedimentary particles reach the Schistes Lustrés P-T conditions (Figure 9a, SL%). Among them, 30–36% are exhumed to the surface, except for the experiment *Ta_*250, for which this proportion reached 51%. In the other experiments (i.e., exp. *Pel*, *Hvel*, *Lvel*, *Qtz*, *Vis_s*, *Sch*., Figure 6), only *Hveland Vis_s* have similar characteristics. The *Pel*, *Lvel*, *Qtz*, *Sch* experiments show P-T-t paths that are globally too "hot" or predict insufficiently low pressure conditions.

[51] Exhumation rates for the experiments best fitting the natural P-T paths (i.e., *Std*, *Ta_*250, *Htc* and *Vis_m*, Figure 10b) range from 1 to 16 mm yr^{-1} (Figure 10). Convergence rates greatly affect exhumation rates (Figure 10c), with exhumation rates of up to 20 mm yr^{-1} in fast convergence experiments (exp. *Hvel*). Exhumation rates decrease drastically after 5 Ma. The early, fast exhumation stages are probably controlled by transient, initial conditions (e.g., initial morphology, thermal profile) before a steady state is achieved, as shown by the thermal stabilization of the accretionary wedge after 5 Ma (Figure 5b). Values obtained *afterward* vary from 1 to 6 mm yr^{-1} (between 5 and 8 Ma) and decrease below 1 mm yr^{-1} after 12 Ma.

8. Discussion

[52] The following key output parameters are compared here with natural data: metamorphic thermal gradients, maximum depths reached in the wedge, the shape of the P-T loops, the characteristic timescale of metamorphism, and exhumation rates and their evolution with time.

8.1. Fit With the Petrology-Based Data From the Schistes Lustrés Complex

[53] Metamorphic thermal gradients obtained in the experiments range between 5 and 8°C km^{-1} (Figure 9), which is close to the 8°C km^{-1} deduced for the western Alps [*Agard et al.*, 2001]. One of the recurrent problems with model-predicted P-T-t paths is that the buried paths are apparently too cold with respect to the estimates derived from petrology data [*Peacock*, 1996]. For example, the temperatures estimated by *Gerya et al.* [2002] and *Stöckhert and Gerya* [2005] also tend to be lower than the "natural" ones by approximately 50–100°C. Our model too does not make an exclusion here (Figure 9b). Several explanations of this common disagreement can be proposed: (1) Some of the coldest paths may exist in nature but are not observed in the field, because the corresponding particles do not reach the surface, (2) the amount of radiogenic heat-producing elements is uncertain and may be underestimated, (3) thermal blanketing may be more important in the wedge than it is accounted for in the models [e.g., *Goffé et al.*, 2003], and (4) frictional shear heating, which would raise the temperature, has been switched off in our experiments (this was done because of the large uncertainty on the value of the energy conversion efficiency multiplier *frac* (Appendix A). Indeed, although thermal conversion efficiency is known to be high for rapid movements (T can locally rise by ~200°C), shear heating is unlikely to be important for the slow convergence movements studied here). On the other hand, there is growing evidence from petrology data that cold P-T paths between 5–8°C km^{-1} exist in nature [e.g., *Tsujimori et al.*, 2006].

[54] Several of our experiments produce realistic morphologies and synthetic P-T-t paths, with isothermal to

Figure 9. (a) P-T-(t) conditions computed by numerical modeling for rocks exhumed in the various experiments. The red, green, and blue dots correspond to P-T outputs at 1, 6, and 11 Ma, respectively. The gray area recalls the P-T domain documented for the paleoaccretionary "Schistes Lustrés" metapelites ([*Agard et al.*, 2001, 2002]; "SL box" of Figure 2a). Percentages refer to the fraction of all stable markers entering the SL box (SL%) and to the fraction of them which are exhumed to the surface (Exh%). (b) P-T constraints for all markers in the wedge. Shaded lines are lowermost temperatures seen by the particles along the burial path in a given experiment. The better the stability of the wedge (see Figure 6), the hotter the low-T boundary of burial paths. Symbols and idealized paths show peak P-T conditions reached by the particles turning in the wedge (P-T loops).

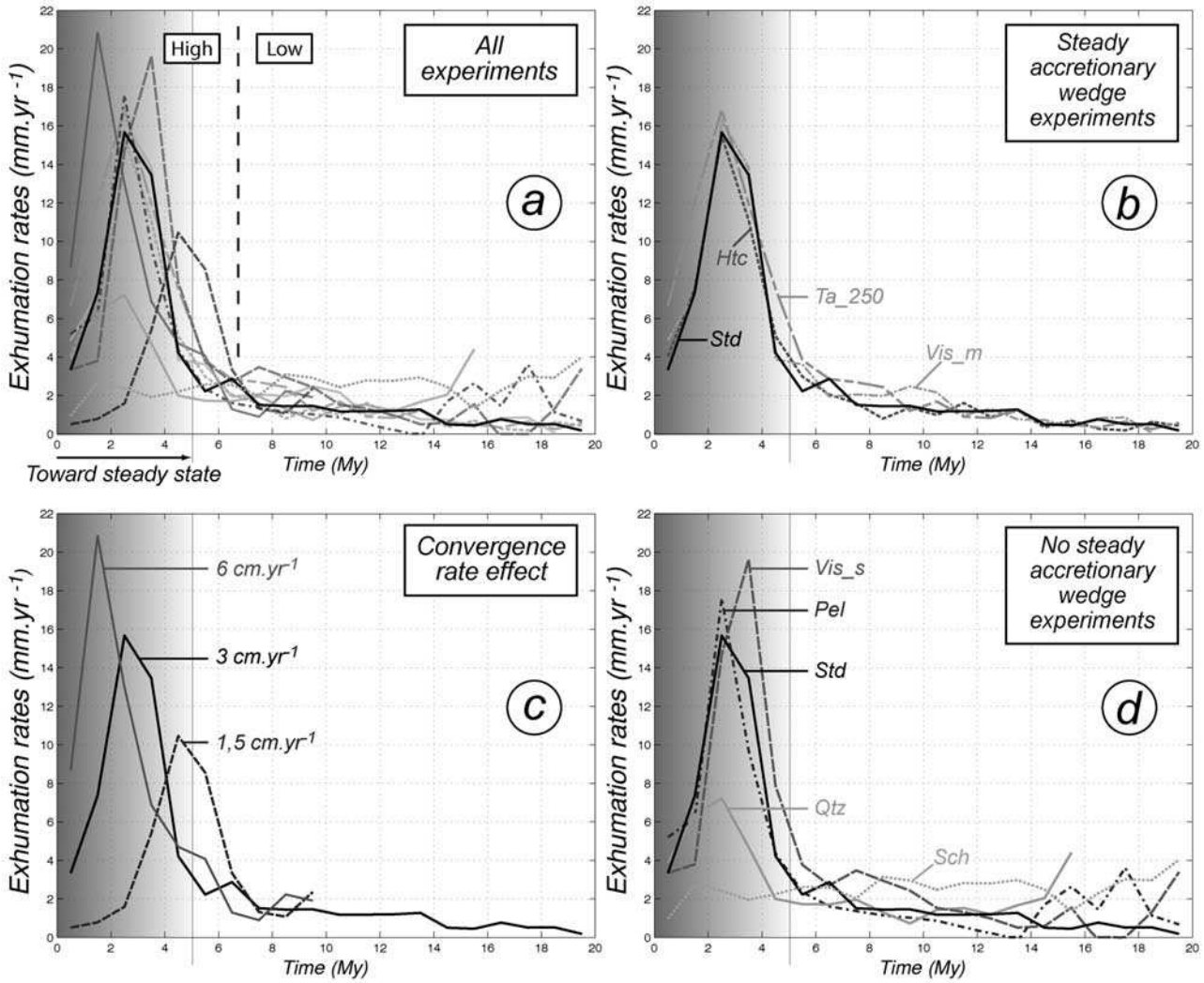

Figure 10. Exhumation rates for all experiments during the 20 Ma modeling (except for models Hvel, Lvel: 0–10 Ma; Qtz: 0–15 Ma). The shaded rectangle recalls the time needed to reach a thermal steady state. Values of exhumation rates decrease to 1–4 mm yr^{-1} after this transition period (~5 Ma).

slightly cooling decompression P-T loops resembling those of the SL complex (Figure 9a). This is particularly the case for the dense, high-viscosity sediments, for which the number of marker points crossing the SL box reaches ~35% (Figure 9a). These paths (Figure 9) show correct maximum P-T values (~20 kbar, ~350–450°C) for all models except for the model with a high-density, aluminium-poor pelite (exp. *Pel*). For the model with a weak lower continental crust (exp. *Qtz*), the fact that the sediment particles stay at depth explains the ''hotter'' values obtained. The best values are again those obtained in the model with the 250 Ma-old continental plate (exp. *Ta*_250).

[55] Our results show that a stable oceanic accretionary wedge such as the one documented for the Liguro-Piemontese Ocean [*Schwartz et al.*, 2000a; *Agard et al.*, 2001] is neither compatible with the presence of a weak lower continental crust (Figure 6j, exp. *Qtz*) nor with large or very slow convergence velocities. Only convergence velocities close to 3 cm yr^{-1} (*Std* simulation) allow for steady state accretion. This value corresponds to average convergent rates inferred from mean worldwide expansion rates over the last 180 Ma (~2.6 cm yr^{-1} [*Cogné and Humler*, 2004]), but is a little high for the western Alps (~2 cm yr^{-1} [*Le Pichon et al.*, 1988]).

[56] During the initial transient period of 5 Ma, calculated exhumation rates (~1–20 mm yr^{-1}, Figure 10) are larger than those inferred from petrological data (~1–5 mm yr^{-1}, Figure 2b). After this period, however, these rates decrease to ~1–6 mm yr^{-1} (Figure 10) and become comparable to ''petrological'' ones. The agreement between the predicted and inferred exhumation rates can be considered as good, given the uncertainties arising from (1) the scatter in pressure estimates (~1–2 kbar), (2) the scatter in phengite closure temperature (~50°C at least [*Villa*, 1998]), (3) the excess of nonradiogenic argon in natural samples [e.g., *Scaillet*, 1996] (see discussion in section 2.2), and (4) the choice of a thermomechanical model setup.

[57] Our results indicate that processes of burial and exhumation to the surface occur within 10–15 Ma, which suggests that cyclic burial-exhumation processes may exist in the sedimentary wedge. Such cycles could account for the fact that radiometric ages of the SL complex mainly span

the range of 38–55 Ma (Figure 2b), though subduction started at ~100 Ma in the western Alps. We speculate that the SL complex may represent sediments buried and exhumed toward the last stages of oceanic subduction, whereas earlier sediments were already exhumed and eroded.

8.2. Parameters Controlling the Exhumation of the Oceanic Crust

[58] The major disagreement with natural observations refers to the fact that no exhumation of the oceanic crust took place in our experiments. Although voluminous parts of the accretionary wedge are generally devoid of oceanic crust (SL complex, Figure 1a, inset), large metamorphosed oceanic crustal bodies are also found in close association with serpentinites [e.g., *Guillot et al.*, 2004], mainly to the east of the SL complex (e.g., Zermatt-Saas, Monviso; see section 2.2).

[59] For this reason, we designed a set of complementary experiments to investigate the conditions allowing for the detachment of the oceanic crust from the mantle and for its incorporation into the accretionary wedge, with the possible help from serpentinization. This is also justified by the existence of seafloor alteration and extensive hydrothermal activity, and the fact that the Liguro-Piemontese Ocean was a low-spreading ocean with seafloor serpentinized peridotites [e.g., *Lagabrielle and Cannat*, 1990]. We therefore have run three versions of the *Std* experiment, assuming (1) a weaker rheology for the oceanic crust (exp. *Oc*_1), (2) a decollement level below the oceanic crust (exp. *Oc*_2), and (3) a serpentinite layer below the oceanic crust (exp. *Oc*_3).

[60] In *Oc*_1 experiment, parameters are the same as for the *Std* experiment, except that the oceanic crust is weaker (viscosity parameter A multiplied by 1000). In experiment *Oc*_2, a weak, 6 km thick layer with constant viscosity of 5.10^{19} Pa s was introduced below the oceanic crust (Figure 11). All others parameters are the same as in the *Std* experiment. Parameters in experiment *Oc*_3 are the same as exp. *Oc*_2 but serpentinite density is taken into account (Figure 3f). Note that the material used in the experiment *Oc*_2 does not correspond to any physical reality but allows us (by comparing it with the experiment *Oc*_3) to test which parameter, viscosity or density, is the most influential.

[61] The results presented in Figure 11 show that no exhumation of oceanic crust occurs in *Oc*_1, which resembles the results of the initial *Std* experiment. Only a limited exhumation from depths of ~20–30 km occurs in *Oc*_2, where slab breakoff ultimately develops. A major change occurs in *Oc*_3, for which density changes in the serpentinite layer (computed with THERIAK, Figure 3f) are taken into account. Figure 11d shows that the serpentinite layer and a part of the oceanic crust detach from the slab, accumulate in the wedge above the BAW and then partly return to the surface.

[62] The key results of experiment *Oc*_3 are the following: (1) A part of the oceanic crust, closely associated with serpentinites, returns to the surface at the rear of the wedge, from depths of 40–50 km, (2) most of the serpentinite layer is forced back to the surface after reaching the depths of 70–100 km (Figures 11d and 11e), (3) P-T paths comparable to those of Monviso and Zermatt-Saas (yet slightly colder) are obtained for markers located in the serpentinite (Figure 11e), (4) exhumation rates are on the order of 3 mm yr^{-1}, and (5) the exhumation of oceanic units is not chiefly controlled by the presence of a low-viscosity material; rather, the volume forces and density contrast at depth between the serpentinites and the wedge matrix seem to play an important role.

8.3. Comparison With Previous Models of Subduction Wedge Processes

[63] Thermomechanical models of subduction wedges were recently implemented in a number of studies with emphasis on the return flow [*Allemand and Lardeaux*, 1997], reaction kinetics [*Guinchi and Ricard*, 1999], deformation modes [*Beaumont et al.*, 1999; *Ellis et al.*, 1999], density contrasts [*Doin and Henry*, 2001], radiogenic heat production [*Goffé et al.*, 2003], deep exhumation and rheological and density changes due to metamorphic reactions [*Burov et al.*, 1999] or hydration-dehydration processes and shear heating [*Gerya et al.*, 2002; *Stöckhert and Gerya*, 2005]. Reasonable exhumation rates (~3 mm yr^{-1} [*Guinchi and Ricard*, 1999]; ~1 mm yr^{-1} [*Allemand and Lardeaux*, 1997]) and P-T paths [*Goffé et al.*, 2003] were obtained, but the exhumation was kinematically prescribed by the model geometry, and many other assumptions and simplifications limit the applicability of these models to other cases.

[64] In this section, our results are compared with the currently most elaborated, essentially ''self-organizing'' thermomechanical exhumation models of Gerya and coworkers (hereafter GCW: [*Gerya et al.*, 2002; *Stöckhert and Gerya*, 2005]). GCW models and our models are broadly similar in that they reproduce the corner flow processes and circulation in the subduction channel [e.g., *Cloos*, 1982], and in that the predicted P-T conditions correctly reproduce the real Alpine P-T paths. The novel features of our experiments refer to the fact that the modeled area is significantly larger, that subduction is not kinematically preimposed and that the surface processes and density changes are taken into account (although it is the case of some of GCW models). The rheology is also explicitly elastic-plastic-viscous and there is no preimposed softening mechanism (e.g., mantle hydration).

[65] Apart from these technical differences, there are also a number of other important differences between the two approaches.

[66] 1. The lateral size of the accretionary wedge in our experiments is significantly larger than in GCW experiments (<10 km). In GCW experiments, the exhumed sediments are dispersed within the oceanic crust as they return to the surface (except for experiments where the degree of serpentinization is low [*Gerya et al.*, 2002, Figures 8 and 9]. Much less mixing occurs in our models, even in the experiment *Oc*_3, which is, we believe, more compatible with the observed extensive metasediment occurrences largely devoid of mafic bodies (Figure 1a, inset; section 2.2).

[67] 2. GCW obtain greater exhumation rates (~5–40 mm yr^{-1} [*Gerya et al.*, 2002]) than in our experiments (~1–6 mm yr^{-1} for the steady part, Figure 10). The latter is more compatible with exhumation velocities on the order of 1–5 mm yr^{-1} for accretionary wedge material in the Alps (Figure 2b).

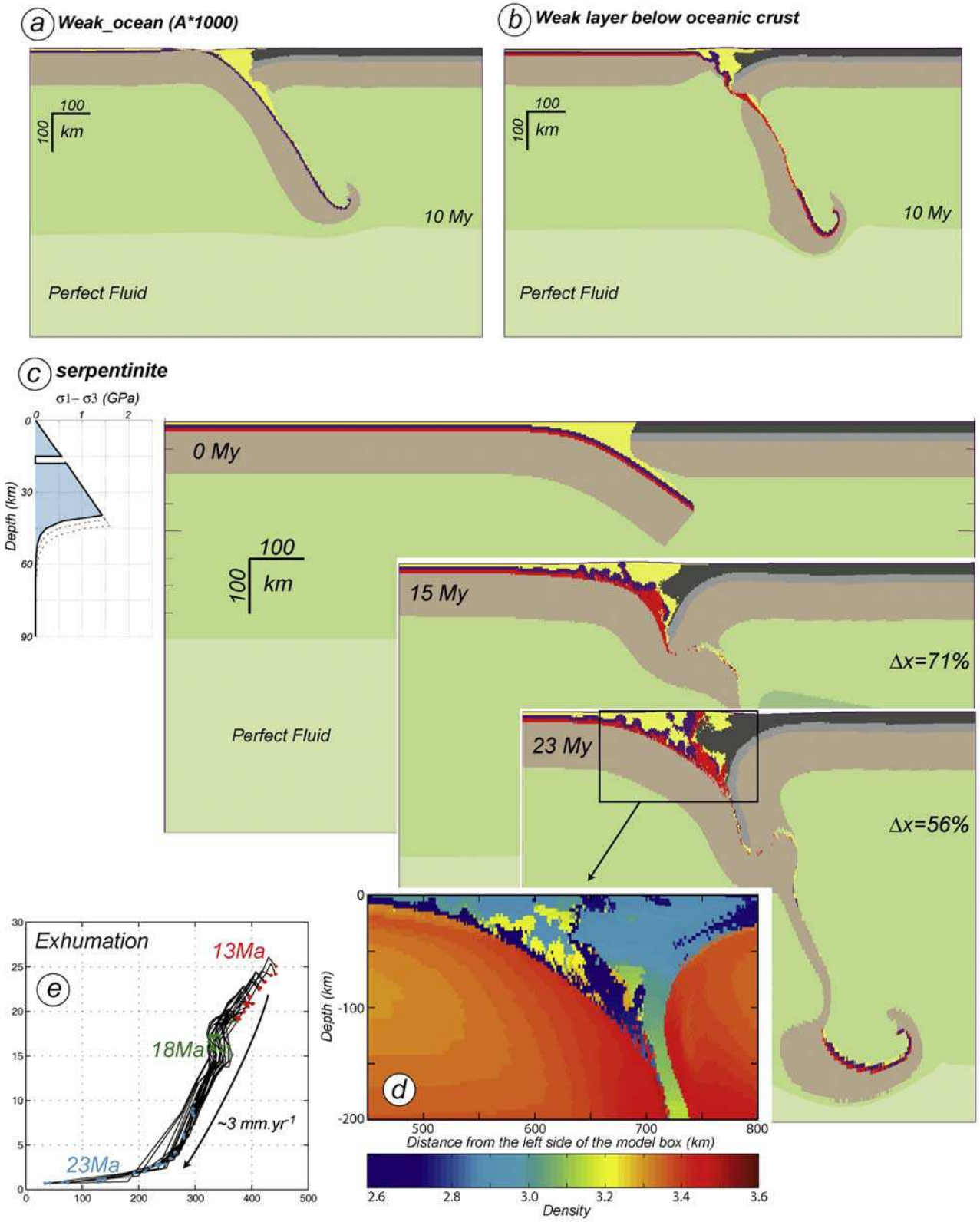

Figure 11. Complementary experiments realized in order to constrain the exhumation of oceanic crust. (a) Exp. *Oc*_1 at 10 Ma. (b) Exp. *Oc*_2 at 10 Ma (weak layer in red). (c) Results obtained for exp. *Oc*_3 at 15 and 23 Ma. (d) Zoom on the density repartition within the accretionary wedge at 23 Ma. (e) Exhumation P-T-t path associated to the exp. *Oc*_3.

[68] 3. Contrary to the GCW models, no exhumation of the oceanic crust takes place in our experiments, except when we introduce a weak serpentinite layer at the base of the oceanic crust (exp. *Oc*_3; see section 8.2). The ability of the oceanic crust to detach from the slab in the GCW experiments stems from the choice of a weak crustal rheology, equivalent to that of serpentinite [*Gerya et al.*, 2002, Figure 2].

[69] 4. Our results demonstrate that exhumation in the accretionary wedge is feasible even without the help from the serpentinization processes. On the other hand, the softening role of serpentinite, either from the slab (this study; exp. *Oc*_3) or from the mantle wedge (GCW experiments), greatly facilitates the exhumation of the oceanic crust. Our experiments therefore account for the fact that in the Alpine case, serpentinite bodies are rare in the SL complex and mainly restricted to eclogitic oceanic units [e.g., *Schwartz et al.*, 2000a, 2001].

[70] 5. Our experiments imply much less continental crustal deformation than *Stöckhert and Gerya* [2005, Figure 2]. These authors argue that the very soft behavior of the crust in their model reproduces the large folds of the central Alpine crystalline nappes [e.g., *Argand*, 1924]. These folds, however, are known to have formed long after subduction, at 30–25 Ma [*Ballèvre and Merle*, 1993; *Stampfli et al.*, 1998] and demonstrate much less rolling-up than modeled by *Stöckhert and Gerya* [2005].

8.4. Applicability to Other Oceanic Accretionary Wedges

[71] Our results can be compared with the burial and exhumation of the HP-LT rocks from the Franciscan Complex, for which a wealth of data are also available. Franciscan rocks represent the prototypical, sediment-rich, fossil accretionary wedge of the east dipping subduction zone operating from ~170 to 100 Ma [*Cloos*, 1985; *Ring and Brandon*, 1999; *Anczkiewicz et al.*, 2004] at the origin of the Sierra Nevada (California) batholith formation [*Ernst*, 1970]. Although the Franciscan subduction was more rapid than the Alpine subduction [*Engebretson et al.*, 1985] and was not followed by collision, some interesting similarities with the Alpine case stand out:

[72] 1. A marked contrast exists between the essentially metasedimentary units, composed of coherent tracts of clastic blueschists [eastern belt; *Cloos*, 1982, 1985; *Ernst*, 1993], and the more internal mud matrix melange where high-grade blueschist and eclogite mafic blocks (knockers) are found in serpentinite diapirs [*Oh and Liou*, 1990; *Wakabayashi*, 1990; *Krogh et al.*, 1994]. The eastern belt is analogous to the Schistes Lustrés [*Agard et al.*, 2001], whereas the melange recalls, yet in a more discontinuous fashion [*Bücher et al.*, 2005], the oceanic crustal bodies and serpentinites of Monviso [*Guillot et al.*, 2004].

[73] 2. Similar P-T gradients are found for Franciscan rocks from the eastern belt but they reached lower maximum P-T values (e.g., ~8 kbar, 200–250°C for the Diablo range [*Ernst*, 1971, 1993]). One can speculate that either the Franciscan wedge was shallower or that the deepest seated rocks are not exposed, probably due to the lack of subsequent collision.

[74] 3. Exhumation velocities on the order of 0.5–1 mm yr^{-1} (mostly erosion-driven, arguably; [*Ring and Brandon*, 1999]) were comparable, yet slightly slower for the Franciscan complex. In general, exhumation mechanisms in accretionary wedges result from a combination of underthrusting and underplating (thus leading to effective circulation in the wedge, whether or not assisted by corner flow), erosion and tectonic thinning [*Platt*, 1986, 1993]. Our predicted rock circulation from Figure 8 is compatible with such processes, but a detailed discussion of the geometry of rock circulation in the wedge [e.g., *Kimura et al.*, 1996; *Ring and Brandon*, 1999] is beyond the scope of the present paper.

[75] 4. The Franciscan subduction zone is known to have cooled during a transient period which lasted ~10–15 Ma [*Peacock*, 1987; *Anczkiewicz et al.*, 2004], whereas this period lasts only ~5 Ma in our experiments. Radiometric constraints for the high-grade blocks corresponding to the oceanic crust suggest, as for the western Alps [*Bücher et al.*, 2005], that they were not exhumed continuously during the subduction process. Contrary to the Alps, however, they apparently detached from the lower plate during the early stages of oceanic subduction [*Cloos*, 1985; *Anczkiewicz et al.*, 2004].

[76] Comparable exhumation velocities are found for the paleoaccretionary wedge of south central Chile (0.6 mm yr^{-1} [*Glodny et al.*, 2005]). Exhumation-related P-T data are unfortunately lacking for most large-scale accretionary wedges such as the Shimanto wedge [*Miyazaki and Okumura*, 2002], the Makran [*McCall*, 1997], and the Barbados.

8.5. Should Overpressure Be Neglected at Depth?

[77] Passive markers permit the tracking of the evolution of pressure with depth (Figure 12) and the estimation of the magnitude of overpressure or underpressure with respect to the lithostatic pressure [*Kamb*, 1961; *Blake et al.*, 1967; *Brace et al.*, 1970]. This question was previously addressed by *Mancktelow* [1995], who considered Bernoulli's dynamic overpressure effect in a subduction channel narrowing with depth and bounded by rigid hanging wall and footwall. *Petrini and Podladchikov* [2000] estimated the possible static and dynamic overpressure that may be built up if the lithosphere is squeezed in pure shear collision mode (i.e., without subduction channel). Both *Mancktelow* [1995] and *Petrini and Podladchikov* [2000] suggested that the total pressure can reach levels as high as twice the lithostatic pressure $P_l = \rho g z$. This problem is of fundamental importance for petrology as it challenges the common method of the estimation of exhumation depth z from pressure assuming the lithostatic pressure gradient:

$$z = \frac{P}{\rho g} \tag{2}$$

[78] Pressure is explicitly computed in our experiments as the total pressure (1/3 of the trace of the full stress tensor). This allows us to verify the applicability of the lithostatic hypothesis (2) doubted in the above-mentioned studies. Comparison of the total pressure and P_l (Figure 12) shows that, down to the depths of 70–80 km inside the accretionary wedge, the lithostatic approximation is valid except for the model with a low convergence rate (exp. *Lvel*). These results recall those already obtained by *Burg and Gerya*

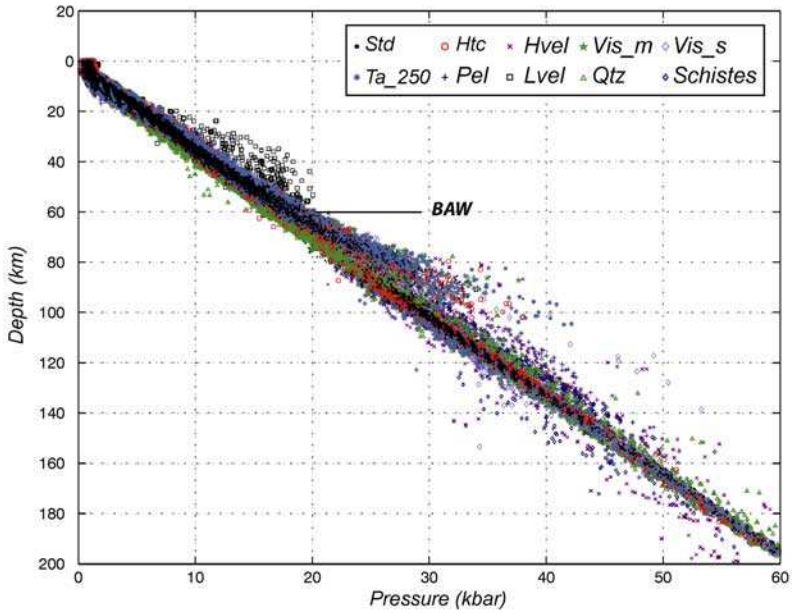

Figure 12. (a) Pressure evolution as a function of depth for all experiments. Within the accretionary wedge; that is, above the bottom of the accretionary wedge (BAW, Figure 2c), no significant over- or under-pressure exists, except for the experiment Pel. At 80–100 km depth the presence of small over- (or under-) pressure can be assigned to the constriction zone in the subduction where stresses are maximum (below the BAW).

[2005]. Within the depth interval of 80–150 km, small underpressures and overpressures (max = 10%) occur in the subduction channel. As the depth interval of 80–150 km does not correspond to that of the blueschists, but rather to the eclogite facies, we infer that tectonic overpressure may be neglected in the interpretations of HP rock exhumation during oceanic subduction. In the experiments, important overpressures may nevertheless be observed outside the subduction channel, inside the competent cores of the subducting and overriding plate as also shown by *Toussaint et al.* [2004].

9. Conclusion

[79] The synthetic P-T-t paths predicted by our thermomechanically and thermodynamically coupled model can be directly compared with the P-T-t paths inferred from the petrology data. This allows new constraints to be placed on the thermomechanical conditions in subduction settings, and better interpretations and validations of the P-T-t paths inferred from the petrology data to be made. The major results (Figure 13) can be summarized as follows:

[80] 1. We have determined the thermomechanical conditions at which stable accretionary wedge morphologies can persist for over 20 Ma. This agrees with the long-term accretion documented for the western Alps. The predicted surface topography evolution, which presents an additional constraint on the model, fits that of the natural oceanic subduction zones with amplitudes lower than 7 km. Predicted accretionary wedge morphologies best reproduce field observations for experiments with a strong continental lower crust and high-viscosity/low-density wedge sediments.

[81] 2. Part of the incoming sedimentary material is buried to middle depths and then dynamically underplated to form a steady state accretionary wedge with a turnover time of burial-exhumation cycles of 10–15 Ma. Within the accretionary wedge, the metasediments follow P-T-t loops that resemble, both in terms of shape (isothermal to slightly cooling paths) and of the predicted P-T conditions (between ~15–20 kbar and 350–400°C), the well documented Schistes Lustrés fossil accretionary wedge. The smooth, progressive increase of the P-T conditions recorded by the particles is consistent with the metamorphic record in the SL complex [*Agard et al.*, 2001]. Metamorphic thermal gradients around 8°C km^{-1} are in a good agreement with the natural values for the western Alps.

[82] 3. Exhumation rates for the metasediments, for the period when a thermally steady accretionary wedge is formed (after ~3–5 Ma), range between 1 and 10 mm yr^{-1} and are <6 mm yr^{-1} after 5 Ma in almost all experiments. These exhumation rates are comparable to the natural ones for the SL complex based on ^{40}Ar–^{39}Ar dating (1–5 mm yr^{-1}).

[83] 4. Exhumation in a sedimentary accretionary wedge is feasible even without intervening serpentinization processes. This result is in line with the occurrence of extensive, continuous metasedimentary outcrops lacking serpentinites. On the other hand, our experiments also confirm the inferences of previous studies [*Gerya et al.*, 2002] concerning the high potential, when applicable, of serpentinization to ease exhumation processes.

[84] 5. The oceanic crust remains attached to the slab in most of the oceanic subduction experiments, preventing exhumation. The rheology that we have assumed for the oceanic crust may be too strong, compared to the soft rheology used in previous studies [*Gerya et al.*, 2002; *Stöckhert and Gerya*, 2005]. Exhumation nevertheless takes place when a weak, low-density serpentinite layer is added below the oceanic crust (exp. *Oc*_3). This mechanism could

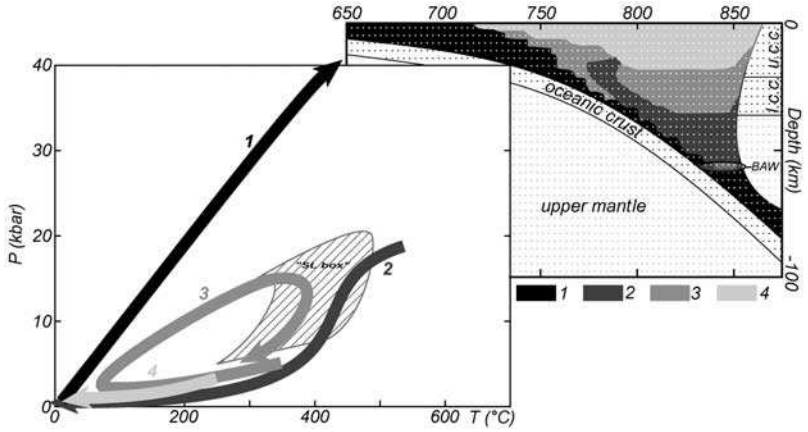

Figure 13. Sketch summarizing the main observations from our experiments. Deepest sedimentary particles (curve 1) close to the oceanic crust are buried down to mantle depths along a cold P-T-t path and never come back to the surface. Particles located just above the BAW at the accretionary wedge basis (curve 2) are exhumed from P-T conditions of 15–20 kbar and 500–600°C to the surface. At the top (curve 4), exhumation is principally driven by erosion processes and underplating of the material below. Between these two levels, particles (curve 3) are underplated and turn in the accretionary wedge. Their P-T-t path is a loop resembling those documented for the natural samples of the Schistes Lustrés complex (Figure 2a).

account for the exhumation of crustal units spatially associated with serpentinites (e.g., Zermatt-Saas, Monviso).

[85] 6. Exhumation mechanisms for oceanic crustal rocks differ from that of the predominant sedimentary material. Large mafic bodies may have been exhumed either during oceanic convergence, because of the existence of underlying serpentinites, or, on the basis of geological observations, later during the locking of continental subduction and exhumation of the European margin.

[86] 7. Contrary to some earlier ideas, overpressures are negligible within the accretionary wedge. Small overpressures (but also underpressures) can be built up below the subduction channel (at ~80–100 km).

Appendix A: Numerical Algorithm

[87] PARA(O)VOZ is a mixed finite volume element/finite difference numerical code based on the FLAC technique [*Cundall and Board*, 1988; *Cundall*, 1989]. It simultaneously solves Newtonian dynamic equations of motion (A1), in a Lagrangian formulation, coupled with visco-elasto-plastic constitutive equations (A2), heat transport equations (A3) and state equation (A4) or its extended thermodynamic version [e.g., *Burov et al.*, 2001; *Le Pourhiet et al.*, 2004].

$$\left\langle \rho_i \frac{\partial^2 \mathbf{u}}{\partial t^2} \right\rangle - div\boldsymbol{\sigma} - \boldsymbol{\rho}_{eff}\mathbf{g} = 0 \tag{A1}$$

$$\frac{D\sigma}{Dt} = F(\sigma, \mathbf{u}, \mathbf{V}, \nabla\mathbf{V}, \ldots T \ldots) \tag{A2}$$

$$\rho_{eff} C_p \partial T/\partial t + \mathbf{u}\,\nabla T - k\,div(\nabla T) - H_r - frac \times \sigma_{\mathrm{II}} \partial\varepsilon_{\mathrm{II}}/\partial t = 0 \tag{A3}$$

assuming adiabatic temperature dependency for density and Boussinesq approximation for thermal body forces:

$$\rho_{eff} = \rho_0(1 - \alpha\Delta T) \quad \text{or} \quad \rho_{eff} = f(P, T) \text{ via THERIAK} \tag{A4}$$

where $\mathbf{u}$, $\boldsymbol{\sigma}$, $\boldsymbol{g}$, k are the respective terms for the velocity, stress, and acceleration due to the body forces and thermal conductivity. The triangular brackets in (A1) specify conditional use of the inertial term: In quasi-static mode, the inertia is dumped using inertial mass scaling [*Cundall*, 1989]. The terms t, ρ_{eff}, C_p, T, H_r, α, $frac \times \sigma_{\mathrm{II}}\partial\varepsilon_{\mathrm{II}}/\partial t$ are respectively time, density, specific heat, temperature, internal heat production, thermal expansion coefficient and shear heating term. The parameter *frac* is an experimentally defined multiplier characterizing the efficiency of conversion of the mechanical energy (set to 0 in our experiments). For radiogenic heat production, we use the common relation $H_r = H_s \exp(-z/h_r)$, where H_s is surface heat production and h_r is the characteristic decay length with depth z [e.g., *Turcotte and Schubert*, 2002]. The terms $\partial/\partial t$, $D\sigma/Dt$, F are a time derivative, an objective (Jaumann) stress time derivative and a functional, respectively. In the Lagrangian framework, the incremental displacements are added to the grid coordinates, allowing the mesh to move and deform with the material. This allows one to solve the large-strain problems by locally using small-strain formulation: On each time step the solution is obtained in local coordinates, which are then updated in the large strain mode. Volume/density changes due to phase transitions are accounted for through the application of equivalent stresses to the affected material elements.

[88] Solution of (A1) provides velocities at mesh points used for computation of element strains and of heat advection $\mathbf{u}\nabla T$ (A3). These strains are used in (A2) to calculate element stresses, and the equivalent forces are used to compute velocities for the next time step.

	continent minerals	%	ocean minerals	%	pelite-1 minerals	%	pelite-2 minerals	%
	Kfs	59.0	Pl	27.6	Phg	31.2	Phg	39.3
	Phg	6.6	Phg	1.1	Chl	28.5	Chl	34.5
Pt 1	Ep	5.7	Omp	12.7	Kln	7.9	a-Qtz	26.2
7.5 kbar	Mag	1.5	Chl	25.5	a-Qtz	32.4		
250°C	Rt	0.3	Ep	14.1				
	a-Qtz	27.0	Lws	9.2				
			Spn	4.2				
			a-Qtz	5.6				
density	**2.73**		**3.01**		**2.86**		**2.94**	
	Kfs	34.5	Phg	1.2	Phg	32.5	Phg	39.4
	Phg	6.9	Omp	35.5	Chl	19.6	Chl	34.6
Pt 2	Omp	16.6	Chl	24.3	Cld	12.9	a-Qtz	26.1
17.5 kbar	Ep	6.0	Ep	16.1	a-Qtz	35.0		
450°C	Mag	1.5	Lws	9.7				
	Rt	0.3	Rt	1.5				
	a-Qtz	34.2	a-Qtz	11.7				
density	**2.89**		**3.21**		**2.97**		**2.97**	
	Kfs	59.3	Pl	32.3	Phg	32.0	Bt	17.2
	Phg	6.4	Bt	0.9	Chl	25.6	Phg	23.8
Pt 3	Ep	5.5	Omp	11.5	Cld	6.4	Chl	26.8
7.5 kbar	Mag	1.5	Chl	25.9	a-Qtz	36.0	a-Qtz	32.2
500°C	Rt	0.3	Ep	18.8				
	a-Qtz	27.0	Spn	4.2				
			a-Qtz	6.4				
density	**2.71**		**2.98**		**2.88**		**2.90**	
	Kfs	34.4	Grt	19.3	Grt	22.1	Grt	24.7
	Phg	6.9	Phg	1.3	Phg	35.5	Bt	19.5
Pt 4	Omp	16.7	Omp	41.9	Cld	8.9	Phg	26.2
22.5 kbar	Ep	6.0	Chl	4.7	a-Qtz	33.6	a-Qtz	29.6
575°C	Mag	1.6	Cld	3.3				
	Rt	0.3	Ep	17.4				
	a-Qtz	34.1	Rt	1.7				
			a-Qtz	10.5				
density	**2.90**		**3.41**		**3.17**		**3.22**	
	Kfs	61.3	Grt	10.5	Grt	11.3	Grt	20.3
	Bt	0.4	Pl	28.8	Bt	19.3	Bt	29.1
Pt 5	Phg	4.7	Bt	1.1	Phg	17.3	Phg	16.8
7.5 kbar	Ep	4.9	Omp	8.6	St	12.1	a-Qtz	33.8
625°C	Mag	1.5	Ep	10.0	a-Qtz	40.0		
	Rt	0.3	Ilm	2.6				
	a-Qtz	26.9	Mag	1.0				
			a-Qtz	10.8				
			Prg	26.6				
density	**2.69**		**3.12**		**3.05**		**3.10**	

	continent minerals	%	ocean minerals	%	pelite-1 minerals	%	pelite-2 minerals	%
	Kfs	34.5	Grt	28.1	Grt	28.0	Grt	25.1
	Phg	6.9	Phg	1.3	Phg	36.2	Bt	18.7
Pt 6	Omp	16.7	Omp	41.3	a-Qtz	32.7	Phg	27.0
25 kbar	Ep	6.0	Ep	17.9	Ky	3.1	a-Qtz	29.2
650°C	Mag	1.6	Rt	1.7				
	Rt	0.3	a-Qtz	9.7				
	a-Qtz	34.1						
density	**2.91**		**3.48**		**3.21**		**3.23**	
	Kfs	60.1	Grt	27.7	Grt	29.4	Grt	21.8
	Phg	6.1	Pl	23.3	Phg	36.1	Bt	25.9
Pt 7	Ep	5.3	Bt	0.3	a-Qtz	34.0	Phg	20.0
17.5 kbar	Mag	1.5	Omp	28.0	Ky	0.6	a-Qtz	32.2
800°C	Rt	0.3	Ep	12.6				
	a-Qtz	26.7	Mag	0.7				
			Rt	1.6				
			a-Qtz	5.6				
density	**2.73**		**3.31**		**3.16**		**3.14**	
	Kfs	68.6	Grt	7.0	Grt	31.6	Grt	32.9
	Bt	0.8	Pl	57.7	b-Qtz	31.4	Bt	14.5
Pt 8	Ep	1.4	Omp	19.4	Sil	9.3	b-Qtz	28.7
10 kbar	Mag	1.9	Opx	12.0	Kfs	27.7	Kfs	23.9
900°C	Rt	0.3	Ilm	0.2				
	b-Qtz	27.1	Mag	2.4				
			Rt	1.4				
density	**2.64**		**3.05**		**3.08**		**3.11**	
	Kfs	34.9	Grt	29.2	Grt	28.4	Grt	27.2
	Phg	7.0	Phg	1.4	Phg	37.0	Bt	15.6
Pt 9	Omp	17.4	Omp	41.1	Coe	30.9	Phg	30.9
30 kbar	Ep	6.2	Ep	17.4	Ky	3.7	Coe	26.4
700°C	Mag	1.6	Rt	1.7				
	Rt	0.3	Coe	9.2				
	Coe	32.6						
density	**3.00**		**3.51**		**3.30**		**3.32**	
	Kfs	42.3	Grt	31.9	Grt	28.9	Grt	23.8
	Phg	6.4	Phg	1.4	Phg	36.2	Bt	21.9
Pt 10	Omp	12.1	Omp	40.0	a-Qtz	33.2	Phg	24.0
27.5 kbar	Ep	5.5	Ep	13.7	Ky	1.7	a-Qtz	30.4
950°C	Mag	1.6	Mag	0.7				
	Rt	0.3	Rt	1.7				
	a-Qtz	31.8	a-Qtz	10.7				
density	**2.85**		**3.46**		**3.19**		**3.19**	

Figure B1. Mineral assemblages and density computed by THERIAK for various P-T conditions for all materials used in the experiments.

[89] All rheological terms are implemented explicitly. The rheology model is serial viscous-elastic-plastic (Table 1). The plastic term is given by explicit Mohr-Coulomb plasticity (nonassociative with zero dilatency) assuming linear Navier-Coulomb criterion. By default, we imply internal friction angle ϕ of 30° and maximal cohesion S of 20 MPa, which best fit the experimental Byerlee's law of rock failure [*Byerlee*, 1978]:

$$\tau = S + \sigma_n \operatorname{tg} \phi \tag{A5}$$

where τ is the shear stress and σ_n is the normal stress. Linear cohesion softening is used for better localization of plastic deformation ε_p ($S(\varepsilon_p) = S_0$ min (0, $1 - \varepsilon_p/\varepsilon_{p0}$) where ε_{p0} is 0.01). Specific properties are applied to soft serpentinized rock [*Hassani and Chéry*, 1996]. The ductile-viscous term is represented by nonlinear power law with three sets of material parameters (Table 1) that correspond to the properties of four lithological layers that include the upper crust (quartz), middle lower crust (quartz diorite), mantle and asthenosphere (olivine):

$$\eta_{\text{eff}} = \left(\frac{\partial \varepsilon}{\partial t}\right)_{\text{II}}^{d(1-n)/n} \left(\text{A}^*\right)^{-1/n} \exp(H/nRT) \tag{A6}$$

where $\left(\frac{\partial \varepsilon}{\partial t}\right)_{\text{II}}^{d} = \left(Inv_{II}\left(\left(\frac{\partial \varepsilon}{\partial t}\right)_{\text{II}}^{d}\right)\right)^{1/2}$ is the effective strain rate and $\text{A}^* = {}^1/_2\text{A} \cdot 3^{(n+1)/2}$ is the material constant, H is the activation enthalpy, R is the gas constant, n is the power law exponent (Table 2). The elastic parameters (Table 1) correspond to commonly inferred values from *Turcotte and Schubert* [2002].

[90] In addition, surface processes are taken into account by diffusing (A7) the topographic elevation h along x using conventional Culling erosion model [*Culling*, 1960] with a diffusion coefficient k_{ero}.

$$\frac{\partial h}{\partial t} = k_{\text{ero}} \frac{\partial^2 h}{\partial x^2} \tag{A7}$$

This simple model is well suited to simulate fan deltas, which can be taken as a reasonably good analogue of typical foreland basin deposits. This model is not well adapted to model slope-dependent long-range sedimentation, yet, it accounts for most important properties of surface processes such as dependency of the erosion/sedimentation rate on the roughness of the relief (surface curvature).

[91] PARA(O)VOZ allows for large displacements and strains in particular owing to an automatic remeshing procedure, which is implemented each time the mesh becomes too distorted to produce accurate results. The remeshing criterion is imposed by a critical angle of grid elements. This angle is set to 10° to reduce frequency of remeshing and thus limit the associated numerical diffusion. The numerical diffusion was constrained by implementation of the passive marker algorithm. This algorithm traces passively moving particles, which are evenly distributed in the initial grid (we use nine particles per grid element, Figure 4). This permits an accurate recovery of stress, phase and other field parameters after each remeshing.

Appendix B: Mineral Assemblages and Density Computed by THERIAK for Various P-T Conditions for All Materials Used in the Experiments

[92] Mineral assemblages are given with weight proportions. Chosen P-T conditions correspond to the points (Pt) of Figure 3. Symbols are given after *Kretz* [1983], except for phengite (Phg) and coesite (Coe). See Figure B1.

Appendix C: Passive Markers and Remeshing

[93] To reduce the computational efforts, we use the already defined trilinear shape functions of the main finite element grid. At initialization, and after each remeshing event, the algorithm seeks for the global element number of the hosting triangular element for each marker. This procedure is fulfilled using the parameters of the trilinear shape functions $\boldsymbol{N}$ (C1).

$$N_i(x,y) = \alpha_i + x\beta_i + y\gamma_i \quad , i \in [1,3] \tag{C1}$$

where x and y are the coordinates. The coefficients α_i, β_i, γ_i of the shape functions are obtained by computing the transformation from the natural coordinates of the isoparametric trilinear triangle element to the global Cartesian coordinates of its nodes (x_1, x_2, x_3, y_1, y_2, y_3):

$$\begin{bmatrix} \alpha_1 & \beta_1 & \gamma_1 \\ \alpha_2 & \beta_2 & \gamma_2 \\ \alpha_3 & \beta_3 & \gamma_3 \end{bmatrix} = \begin{bmatrix} 1 & 1 & 1 \\ x_1 & x_2 & x_3 \\ y_1 & y_2 & y_3 \end{bmatrix}^{-1} \tag{C2}$$

If the marker *imar* is found inside the element, then the values of all three local coordinates have to be included between 0 and 1 and their sum be equal to 1 (C3):

$$\text{i.e.}, \forall i = 1,3 \quad |N_i(x_{imar}, y_{imar}) - 1/2| \le 1/2 + \varepsilon_{tol}$$
$$\text{and} \left| \sum_{i=1}^{3} N_i(x_{imar}, y_{imar}) - 1 \right| \le \varepsilon_{tol} \tag{C3}$$

where ε_{tol} is tolerated error and x_{imar} and y_{imar} are the global coordinates of the *imar* marker. Once the marker is found, the interpolation weights L_i of the nodal values at the location of the marker are calculated (C4).

$$L_i(imar) = N_i(x_{imar}, y_{imar}) \tag{C4}$$

The nodal values, as well as the global number of the triangle hosting the marker, are stored in memory. This enables us to compute coordinates, temperature and velocity of the marker from the nodal values of the element (C5) only when it is needed (i.e., for output and before remeshing).

$$X(imar) = \sum_{i=1,3} X_i L_i(imar) \tag{C5}$$

The pressure does not need to be interpolated using markers but is taken from the four subtriangles of the mesh quadrilaterals to avoid numerical over or under pressure.

[94] **Acknowledgments.** We thank T. V. Gerya, C. J. Warren, and G. Rosenbaum for careful reviews which largely contributed to improvement of the final version of the manuscript.

References

Agard, P. and M. Lemoine (2005), *Faces of the Alps. Structure and Geodynamic Evolution*, 48 pp., Comm. for the Geol. Map of the World, Paris.

Agard, P., L. Jolivet, and B. Goffé (2001), Tectonometamorphic evolution of the Schistes Lustrés complex: Implications for the exhumation of HP and UHP rocks in the western Alps, *Bull. Fr. Geol. Soc.*, *172*(5), 617–636.

Agard, P., P. Monié, L. Jolivet, and B. Goffé (2002), Exhumation of the Schistes Lustrés complex: In situ laser probe $^{40}Ar/^{39}Ar$ constraints and implications for the western Alps, *J. Metamorph. Geol.*, *20*(6), 599–618.

Allemand, P., and J. M. Lardeaux (1997), Strain partitioning and metamorphism in a deformable orogenic wedge: Application to the Alpine belt, *Tectonophysics*, *280*, 157–169.

Amato, J. F., C. M. Johnson, L. P. Baumgartner, and B. L. Beard (1999), Rapid exhumation of the Zermatt-Saas ophiolite deduced from high-precision Sm-Nd and Rb-Sr geochronology, *Earth Planet. Sci. Lett.*, *171*, 425–438.

Anczkiewicz, R., J. P. Platt, M. F. Thirlwall, and J. Wakabayashi (2004), Franciscan subduction off to a slow start: Evidence from high-precision Lu–Hf garnet ages on high grade-blocks, *Earth Planet. Sci. Lett.*, *225*, 147–161.

Argand, E. (1924), La tectonique de l'Asie, in *Proceedings of the 13th International Geological Congress Brussels*, pp. 171–372, Vaillant-Carmanne, Liège.

Arnaud, N. O., and S. P. Kelley (1995), Evidence for excess argon during high pressure metamorphism in the Dora Maira massif (western Alps, Italy), using an ultra-violet laser ablation microprobe $^{40}Ar-^{39}Ar$ technique, *Contrib. Mineral. Petrol.*, *121*, 1–11.

Avouac, J. P., and E. B. Burov (1996), Erosion as a driving mechanism of intracontinental mountain growth, *J. Geophys. Res.*, *101*, 17,747–17,769.

Ballèvre, M., and O. Merle (1993), The Combin fault: Compressional reactivation of a Late Cretaceous-Early Tertiary detachment fault in the western Alps, *Schw. Mineral. Petrogr. Mitt.*, *73*, 205–227.

Barnicoat, A. C., and N. Fry (1986), High-pressure metamorphism of the Zermatt-Saas ophiolite zone, Switzerland, *J. Geol. Soc. London*, *143*, 603–618.

Baxter, E. F., D. J. DePaolo, and P. R. Renne (2002), Spatially correlated anomalous $^{40}Ar/^{39}Ar$ "age" variations in biotites about a lithologic contact near Simplon Pass, Switzerland: A mechanistic explanation for excess Ar, *Geochim. Cosmochim. Acta*, *66*(6), 1067–1083.

Beaumont, C., P. Fullsack, and J. Hamilton (1994), Styles of crustal deformation in compressional orogens caused by subduction of the underlying lithosphere, *Tectonophysics*, *232*(1–4), 119–132.

Beaumont, C., S. Ellis, and A. Pfiffner (1999), Dynamics of sediment subduction-accretion at convergent margins: Short-term modes, long-term deformation, and tectonic implications, *J. Geophys. Res.*, *104*, 17,573–17,601.

Beaumont, C., R. A. Jamieson, M. H. Nguyen, and B. Lee (2001), Himalayan tectonics explained by extrusion of a low-viscosity crustal channel coupled to focus surface denudation, *Nature*, *414*, 738–742.

Berman, R. G. (1988), Internally-consistent thermodynamic data for minerals in the system Na_2O-K_2O-CaO-MgO-FeO-Fe_2O_3-Al_2O_3-SiO_2-TiO_2-H_2O-CO_2, *J. Petrol.*, *29*(2), 445–522.

Berman, R. G. (1991), Thermobarometry using multi-equilibrium calculations: A new technique, with petrological applications, *Can. Mineral.*, *29*, 833–855.

Blake, M. C., W. P. Irwin, and R. G. Coleman (1967), Upside-down metamorphic zonation, blueschist facies, along a regional thrust in California and Oregon, *U.S. Geol. Surv. Prof. Pap.*, *575*(C), 307–328.

Bousquet, R., B. Goffé, P. Henry, X. Le Pichon, and C. Chopin (1997), Kinematic, thermal and petrological model of the central Alps: Lepontine metamorphism in the upper crust and eclogitisation of the lower crust, *Tectonophysics*, *273*(1–2), 105–127.

Bowtell, S., R. A. Cliff, and A. C. Barnicoat (1994), Sm-Nd isotopic evidence of the age of eclogitization in the Zermatt-Saas ophiolite, *J. Metamorph. Geol.*, *12*, 187–196.

Brace, W. F., W. G. Ernst, and R. W. Kallberg (1970), An experimental study of tectonic overpressure in Franciscan rocks, *Geol. Soc. Am. Bull.*, *81*, 1325–1338.

Brandon, M. T., M. K. Roden-Tice, and J. I. Garver (1998), Late Cenozoic exhumation of the Cascadia accretionary wedge in the Olympic Mountains, NW Washington State, *Geol. Soc. Am. Bull.*, *110*, 985–1009.

Brouwer, F. M., R. L. M. Vissers, and W. M. Lamb (2002), Structure and metamorphism of the Gran Paradiso massif, western Alps, Italy, *Contrib. Mineral. Petrol.*, *143*, 450–470.

Bücher, K. and M. Frey (1994), *Petrogenesis Metamorphic Rocks*, 318 pp., Springer-Verlag, Berlin.

Bücher, K., Y. Fazis, C. De Capitani, and R. Grapes (2005), Blueschists, eclogites, and decompression assemblages of the Zermatt-Saas ophiolite: High-pressure metamorphism of subducted Tethys lithosphere, *Am. Mineral.*, *90*, 821–835.

Burg, J. P., and T. V. Gerya (2005), The role of viscous heating in Barrovian metamorphism of collisional orogens: Thermomechanical models and application to the Lepontine Dome in the central Alps, *J. Metamorph. Geol.*, *23*, 75–95.

Burov, E., and A. B. Watts (2006), The long-term strength of continental lithosphere: "Jelly-sandwich" or "crème-brûlée"?, *GSA Today*, *16*(1), 4–10.

Burov, E., Y. Podladchikov, G. Grandjean, and J. P. Burg (1999), Thermomechanical approach to validation of deep crustal and lithospheric structures inferred from multidisciplinary data: Application to the western and northern Alps, *Terra Nova*, *11*, 124–131.

Burov, E. B., L. Jolivet, L. Le Pourhiet, and A. Poliakov (2001), A thermomechanical model of exhumation of HP and UHP metamorphic rocks in Alpine mountain belts, *Tectonophysics*, *342*, 113–136.

Byerlee, J. D. (1978), Friction of rocks, *Pure Appl. Geophys.*, *116*, 615–629.

Carmichael, R. S. (1989), *Practical Handbook of Physical Properties of Rocks and Minerals*, 741 pp., CRC Press, Florida.

Carter, N. L., and M. C. Tsenn (1987), Flow properties of continental lithosphere, *Tectonophysics*, *136*, 27–63.

Chapple, W. M. (1978), Mechanics of thin-skinned fold-and-thrusts belts, *Geol. Soc. Am. Bull.*, *89*, 1189–1198.

Chemenda, A. I., M. Mattauer, J. Malavieille, and A. N. Bokun (1995), A mechanism for syn-collision rock exhumation and associated normal faulting: Results from physical modelling, *Earth Planet. Sci. Lett.*, *132*, 225–232.

Chopin, C. (1984), Coesite and pure pyrope in high-grade blueschists of the western Alps: A first record and some consequences, *Contrib. Mineral. Petrol.*, *86*, 107–118.

Chopin, C. (2003), Ultrahigh-pressure metamorphism: Tracing continental crust into the mantle, *Earth and Planet Science Lett.*, *212*, 1–14.

Chopin, C., C. Henry, and A. Michard (1991), Geology and petrology of the coesite-bearing terrain, Dora Maira massif, western Alps, *Eur. J. Mineral.*, *3*, 263–291.

Cliff, R. A., A. C. Barnicoat, and S. Inger (1998), Early Tertiary eclogite facies metamorphism in the Monviso Ophiolite, *J. Metamorph. Geol.*, *16*(3), 447–455.

Cloos, M. (1982), Flow melanges: Numerical modelling and geologic constraints on their origin in the Franciscan subduction complex, California, *Geol. Soc. Am. Bull.*, *93*, 330–345.

Cloos, M. (1985), Thermal evolution of convergent plate margins: Thermal modeling and reevaluation of isotopic Ar-Ages for blueschists in the Franciscan complex of California, *Tectonics*, *4*(5), 421–433.

Cloos, M., and R. L. Shreve (1988), Subduction-channel model of prism accretion, melange formation, sediment subduction, and subduction erosion at convergent plate margins: 2. Implications and discussion, *Pure Appl. Geophys.*, *128*, 501–545.

Cogné, J. P., and E. Humler (2004), Temporal variation of oceanic spreading and crustal production rates during the last 180 My, *Earth Planet. Sci. Lett.*, *227*(3–4), 427–439.

Coward, M. and D. Dietrich (1989), Alpine tectonics: An overview, in *Alpine Tectonics*, edited by M. P. Coward, D. Dietrich, and R. G. Park, pp. 1–29, *Geol. Soc. Spec. Publ.*, *45*, 1–29.

Culling, W. E. H. (1960), Analytical theory of erosion, *J. Geol.*, *68*, 333–336.

Cundall, P. A. (1989), Numerical experiments on localization in frictional materials, *Ing. Arch.*, *59*, 148–159.

Cundall, P. A. and M. Board (1988), A microcomputer program for modelling large-strain plasticity problems, in *Numerical Methods in Geomechanics, Innsbruck 1988*, edited by G. Swoboda, pp. 2101–2108, A. A. Balkema, Rotterdam.

Dahlen, F. A., and J. Suppe (1988), Mechanics, growth and erosion of mountain belts, *Geol. Soc. Am. Spec. Pap.*, *218*, 161–178.

Dahlen, F. A. (1990), Critical taper model of fold-and-thrust belts and accretionary wedges, *Annu. Rev. Earth Planet. Sci.*, *18*, 55–99.

Davies, J. H. (1999), Simple analytic model for subduction zone thermal structure, *Geophys. J. Int.*, *139*, 823–828.

Davis, D. M., J. Suppe, and F. A. Dahlen (1983), Mechanics of fold-and-thrust belts and accretionary wedges, *J. Geophys. Res.*, *88*(B2), 1153–1172.

De Capitani, C. (1994), *Gleichgewichts-Phasendiagramme: Theorie und Software*, *Beih. z. Eur. J. Mineral.*, *72*, *Jahrestagung der Dtsch. Mineral. Ges.*, *6*, 48 pp.

De Capitani, C., and T. H. Brown (1987), The computation of chemical equilibrium in complex systems containing non-ideal solutions, *Geochim. Cosmochim. Acta*, *51*, 2639–2652.

Dercourt, J., L. E. Ricou, and B. Vrielinck (1993), *Atlas Tethys Palaeo Environmental Maps*, 307 pp., Gauthier-Villars, Paris.

De Wever, P., and R. Caby (1981), Datation de la base des schistes lustrés postophiolitiques par des radiolaires (Oxfordien-Kimmeridgien moyen) dans les Alpes Cottiennes (Saint Véran, France), *Compte rendu de l'académie des Sciences de Paris*, *292*, 467–472.

Déverchère, J., C. Petit, N. Gileva, N. Radziminovitch, V. Melnikova, and V. Sank'kov (2001), Depth distribution of earthquakes in the Baïkal rift system and its implications for the rheology of the lithosphere, *Geophys. J. Int.*, *146*(3), 714–730.

Deville, M., S. Fudral, Y. Lagabrielle, M. Marthaler, and M. Sartori (1992), From oceanic closure to continental collision: A synthesis of the "Schistes Lustrés" metamorphic complex of the western Alps, *Geol. Soc. Am. Bull.*, *104*, 127–139.

Doin, M. P., and P. Henry (2001), Subduction initiation and continental crust recycling: The roles of rheology and eclogitization, *Tectonophysics*, *342*, 163–191.

Duchêne, S., J. M. Lardeaux, and F. Albarède (1997a), Exhumation of eclogites: Insights from depth-time path analysis, *Tectonophysics*, *280*(1–2), 125–140.

Duchêne, S., J. Blichert-Toft, B. Luais, J. M. Lardeaux, P. Télouk, and F. Albarède (1997b), The Lu-Hf Dating of Alpine Eclogites, *Nature*, *387*, 586–589.

Ellis, S., C. Beaumont, and O. A. Pfiffner (1999), Geodynamic models of crustal-scale episodic tectonic accretion and underplating in subduction zones, *J. Geophys. Res.*, *104*, 15,169–15,190.

Engebretson, D. G., A. Cox, and R. G. Gordon (1985), Relative motions between oceanic and continental plates in the Pacific basin, *Spec. Pap. Geol. Soc. Am.*, *206*, 59 pp.

Ernst, W. G. (1970), Tectonic contact between the Franciscan melange and Great Valley sequence, crustal expression of a Late Mesozoic Benioff zone, *J. Geophys. Res.*, *75*, 886–902.

Ernst, W. G. (1971), Petrologic reconnaissance of Franciscan metagraywackes from the Diablo range, central California coast ranges, *J. Petrol.*, *12*(2), 413–437.

Ernst, W. G. (1993), Metamorphism of Franciscan tectonostratigraphic assemblage, Pacheco Pass area, east-central Diablo Range, California coast ranges, *Geol. Soc. Am. Bull.*, *105*, 618–636.

Ernst, W. G., and G. V. Dal Piaz (1978), Mineral parageneses of eclogitic rocks and related mafic schists of the Piemonte ophiolite nappe, Breuil-St. Jacques area, Italian western Alps, *Am. Mineral.*, *63*, 621–640.

Frey, M., J. Desmons, and F. Neubauer (1999), The new metamorphic map of the Alps, *Schw. Mineral. Petrogr. Mitteil.*, *79*(1), spec. vol., 230 pp.

Gebauer, D., H. P. Schertl, M. Brix, and W. Schreyer (1997), 35 Ma old ultrahigh-pressure metamorphism and evidence for very rapid exhumation in the Dora Maira massif, western Alps, *Lithos*, *41*(1), 5–24.

Gerya, T. V., and D. A. Yuen (2003), Rayleigh-Taylor instabilities from hydration and melting propel "cold plumes" at subduction zones, *Earth Planet. Sci. Lett.*, *212*, 47–62.

Gerya, T. V., B. Stöckhert, and A. L. Perchuk (2002), Exhumation of high-pressure metamorphic rocks in a subduction channel: A numerical simulation, *Tectonics*, *21*(6), 1056, doi:10.1029/2002TC001406.

Gerya, T. V., D. A. Yuen, and W. V. Maresch (2004), Thermomechanical modelling of slab detachment, *Earth Planet. Sci. Lett.*, *226*, 101–116.

Gerya, T. V., J. A. D. Connolly, D. A. Yuen, W. Gorczyk, and A. M. Capel (2006), Seismic implications of mantle wedge plumes, *Phys. Earth Planet. Interiors*, *156*(1–2), 59–74.

Gillet, P., and B. Goffé (1988), On the significance of aragonite occurrence in the western Alps, *Contrib. Mineral. Petrol.*, *99*, 70–81.

Glodny, J., J. Lohrmann, H. Echtler, K. Gräfe, W. Seifert, S. Collao, and O. Figueroa (2005), Internal dynamics of a paleoaccretionary wedge: Insights from combined isotope tectonochronology and sandbox modelling of the south-central Chilean forearc, *Earth Planet. Sci. Lett.*, *231*(1–2), 23–39.

Goetze, C., and B. Evans (1979), Stress and temperature in the bending lithosphere as constrained by experimental rock mechanics, *Geophys. J. R. Astron. Soc.*, *59*, 463–478.

Goffé, B., and C. Chopin (1986), High-pressure metamorphism in the western Alps: Zoneography of metapelites, chronology and consequences, *Schw. Mineral. Petrogr. Mitteil.*, *66*, 41–52.

Goffé, B., and B. Velde (1984), Contrasted metamorphic evolutions in thrusted cover units of the Briançonnais zone (French Alps): A model for the conservation of HP-LT metamorphic mineral assemblages, *Earth Planet. Sci. Lett.*, *68*, 351–360.

Goffé, B., R. Bousquet, P. Henry, and X. Le Pichon (2003), Effect of the chemical composition of the crust on the metamorphic evolution of orogenic wedges, *J. Metamorph. Geol.*, *21*, 123–141.

Gorczyk, W., T. V. Gerya, J. A. D. Connolly, D. A. Yuen, and M. Rudolph (2006), Large-scale rigid-body rotation in the mantle wedge and its implications for seismic tomography, *Geochem. Geophys. Geosyst.*, *7*, Q05018, doi:10.1029/2005GC001075.

Guillot, S., S. Schwartz, K. Hattori, A. Auzende, and J. Lardeaux (2004), The Monviso ophiolitic massif (western Alps), a section through a serpentinite subduction channel, in *Evolution of the Western Alps: Insights From Metamorphism, Structural Geology, Tectonics and Geochronology*, edited by M. Beltrando et al., *J. Virtual Explorer*, vol. 16, pap. 3, electronic ed., ISSN:1441-8142.

Guinchi, C., and Y. Ricard (1999), High-pressure/low-temperature metamorphism and the dynamic of an accretionary wedge, *Geophys. J. Int.*, *136*, 620–628.

Gunnell, Y. (2000), Apatite fission track thermochronology: An overview of its potential and limitations in geomorphology, *Basin Res.*, *12*(2), 115–132.

Hassani, R., and J. Chéry (1996), Anelasticity explains topography associated with Basin and Range normal faulting, *Geology*, *24*, 1095–1098.

Henry, C., A. Michard, and C. Chopin (1993), Geometry and structural evolution of ultra-high pressure and high pressure rocks from the Dora Maira massif, western Alps, *J. Struct. Geol.*, *15*, 965–981.

Heuret, A., and S. Lallemand (2005), Plate motions, slab dynamics and back-arc deformation, *Phys. Earth Planet. Interiors*, *149*, 31–51.

Hofmann, A. (1988), Chemical differentiation of the Earth: The relationship between mantle, continental crust, and oceanic crust, *Earth Planet. Sci. Lett.*, *90*, 297–314.

Holland, T. J. B., and R. Powell (1998), An internally consistent thermodynamic dataset for phases of petrological interest, *J. Metamorph. Geol.*, *16*, 309–343.

Hurford, A. J., and J. C. Hunziker (1989), A revised thermal history for the Gran Paradiso massif, *Schw. Mineral. Petrogr. Mitteil.*, *69*, 319–329.

Inger, S., W. Ramsbotham, R. A. Cliff, and D. C. Rex (1996), Metamorphic evolution of the Sesia-Lanzo zone, western Alps: Time constraints from multi-system geochronology, *Contrib. Mineral. Petrol.*, *126*, 152–168.

Jackson, J. (2002), Strength of continental lithosphere: Time to abandon the jelly sandwich, *GSA Today*, 4–10.

Jamieson, R. A., C. Beaumont, P. Fullsack, and B. Lee (1998), Barrovian regional metamorphism: Where's the heat?, in *What Controls Metamorphism and Metamorphic Reactions?*, edited by P. Treloar and P. O'Brien, *Geol. Soc. London Spec. Publ.*, *138*, 23–51.

Jolivet, L., C. Faccenna, B. Goffé, E. Burov, and P. Agard (2003), Subduction tectonics and exhumation of high-pressure metamorphic rocks in the Mediterranean orogens, *Am. J. Sci.*, *303*(5), 353–409.

Kamb, W. B. (1961), The thermodynamic theory of nonhydrostatically stressed solids, *J. Geophys. Res.*, *66*, 259–271.

Karato, S. (1998), Effects of pressure on plastic deformation of polycrystalline solids: Some geological applications, *Mat. Res. Soc. Symp. Proc.*, *499*, 3–14.

Karato, S. I., M. S. Paterson, and J. D. FitzGerald (1986), Rheology of synthetic olivine aggregates: Influence of the grain size and water, *J. Geophys. Res.*, *91*, 8151–8176.

Kimura, G., S. Maruyama, Y. Isozaki, and M. Terabayashi (1996), Well-preserved underplating structure of the jadeitized Franciscan complex, Pacheco Pass, California, *Geology*, *24*(1), 75–78.

Kohlstedt, D. L., B. Evans, and S. J. Mackwell (1995), Strength of the lithosphere: Constraints imposed by laboratory experiments, *J. Geophys. Res.*, *100*(B9), 17,587–17,602.

Kretz, R. (1983), Symbols for rock-forming minerals, *Am. Mineral.*, *68*, 277–279.

Krogh, E. J., C. W. Oh, and J. G. Liou (1994), Polyphase and anticlockwise P-T evolution for Franciscan eclogites and blueschists from Jenner, California, USA, *J. Metamorph. Geol.*, *12*, 121–134.

Lagabrielle, Y., and M. Cannat (1990), Alpine Jurassic ophiolites resemble the modern central Atlantic basement, *Geology*, *18*(4), 319–322.

Lapen, T. J., C. M. Johnson, L. P. Baumgartner, N. J. Mahlen, B. L. Beard, and J. M. Amato (2003), Burial rates during prograde metamorphism of an ultra-high-pressure terrane: An example from Lago di Cignana, western Alps, Italy, *Earth Planet. Sci. Lett.*, *215*(1–2), 57–72.

Lardeaux, J. M., and M. I. Spalla (1991), From granulites to eclogites in the Sesia zone (Italian western Alps): A record of the opening and closure of the Piedmont Ocean, *J. Metamorph. Geol.*, *9*, 35–59.

Lemoine, M., and P. Tricart (1986), Les Schistes Lustrés piémontais des Alpes Occidentales: Approche stratigraphique, structurale et sédimentologique, *Eclogae Geol. Helvetiae*, *79*, 271–294.

Lemoine, M., M. Marthaler, J. M. Caron, M. Sartori, S. Amaudric Du Chaffaut, T. Dumont, A. Escher, H. Masson, R. Polino, and P. Tricart (1984), Découverte de foraminifères planctoniques du Crétacé supérieur dans les schistes lustrés du Queyras (Alpes occidentales). Conséquences paléogéographiques et tectoniques, *Comptes Rendus de l'Academie des Sciences*, *229*, 727–732.

Lemoine, M., et al. (1986), The continental margin of the Mesozoic Tethys in the western Alps, *Mar. Pet. Geol.*, *3*, 179–199.

Le Pichon, X., F. Bergerat, and M. J. Roulet (1988), Plate kinematics and tectonics leading to the Alpine belt formation: A new analysis, *Geol. Soc. Am. Spec. Pap.*, *218*, 111–131.

Le Pourhiet, L., E. Burov, and I. Moretti (2004), Rifting through a stack of inhomogeneous thrusts (the dipping pie concept), *Tectonics*, *23*, TC4005, doi:10.1029/2003TC001584.

Mackwell, S. J., M. E. Zimmerman, and D. L. Kohlstedt (1998), High-temperature deformation of dry diabase with applications to tectonics on Venus, *J. Geophys. Res.*, *103*, 975–984.

Mancktelow, N. S. (1995), Nonlithostatic pressure during sediment subduction and the development and exhumation of high pressure metamorphic rocks, *J. Geophys. Res.*, *100*(B1), 571–583.

McCall, G. J. H. (1997), The geotectonic history of the Makran and adjacent areas of southern Iran, *J. Asian Earth Sci.*, *15*(6), 517–531.

Messiga, B., J. R. Kienast, G. Rebay, M. P. Riccardi, and R. Tribuzio (1999), Cr-rich magnesiochloritoid eclogites from the Monviso ophiolites (western Alps, Italy), *J. Metamorph. Geol.*, *17*(3), 287–299.

Meyer, J. (1983), Mineralogie und Petrologie Des Allalin Gabbros, Univ. of Basel, Switzerland.

Michard, A., B. Goffé, C. Chopin, and C. Henry (1996), Did the western Alps develop through an Oman-type stage? The geotectonic setting of high pressure metamorphism in two contrasting Thethyan transects, *Eclogae Geol. Helvetiae*, *89*(1), 43–80.

Miyazaki, K., and K. Okumura (2002), Thermal modelling in shallow subduction: An application to low P/T metamorphism of the Cretaceous Shimanto Accretionary Complex, Japan, *J. Metamorph. Geol.*, *20*, 441–452.

Müller, W. (2003), Strengthening the link between geochronology, textures and petrology, *Earth Planet. Sci. Lett.*, *206*(3–4), 237–251.

Oberhänsli, R., et al. (2004), *Metamorphic Structure of the Alps*, map, 1:1,000,000, Comm. for the Geol. Map of the World (UNESCO), Paris.

Oh, C. W., and J. G. Liou (1990), Metamorphic evolution of two different eclogites in the Franciscan Complex, California, USA, *Lithos*, *25*, 41–53.

Parsons, B., and T. G. Sclater (1977), An analysis of the variation of ocean floor bathymetry and heat flow with age, *J. Geophys. Res.*, *82*, 803–827.

Peacock, S. M. (1987), Creation and preservation of subduction-related metamorphic gradients, *J. Geophys. Res.*, *92*(12), 736–781.

Peacock, S. M. (1996), Thermal and Petrologic structure of subduction zones, in *Subduction: Top to Bottom*, edited by G. E. Bebout et al., pp. 119–133, *Geophys. Monogr. Ser.*, *96*, AGU, Washington, D. C.

Petrini, K., and Y. Podladchikov (2000), Lithospheric pressure-depth relationship in compressive regions of thickened crust, *J. Metamorph. Geol.*, *18*, 67–77.

Pfiffner, O. A., S. Ellis, and C. Beaumont (2000), Collision tectonics in the Swiss Alps: Insight from geodynamic modeling, *Tectonics*, *19*(6), 1065–1094.

Philippot, P. (1990), Opposite vergence of nappes and crustal extension in the French-Italian western Alps, *Tectonics*, *9*, 1143–1164.

Philippot, P., and J. R. Kienast (1989), Chemical-microstructural changes in eclogite-facies shear zones (Monviso, western Alps, north Italy) as indicators of strain history and the mechanism and scale of mass transfer, *Lithos*, *23*(3), 179–200.

Platt, J. P. (1986), Dynamics of orogenic wedges and the uplift of high-pressure metamorphic rocks, *Geol. Soc. Am. Bull.*, *97*, 1037–1053.

Platt, J. P. (1993), Exhumation of high-pressure rocks: A review of concept and processes, *Terra Nova*, *5*, 119–133.

Pognante, U. (1991), Petrological constraints on the eclogite- and blueschist-facies metamorphism and P-T-t paths in the western Alps, *J. Metamorph. Geol.*, *9*, 5–17.

Poliakov, A., Y. Podladchikov, and C. Talbot (1993), Initiation of salt diapirs with frictional overburden: Numerical experiments, *Tectonophysics*, *228*, 199–210.

Polino, R. (1984), Les séries océaniques du Haut val de Suse (Alpes Cottiennes): Analyse des couvertures sédimentaires, *Ofioliti*, *9*, 547–554.

Pysklywec, R. N., C. Beaumont, and P. Fullsack (2002), Lithospheric deformation during the early stages of continental collision: Numerical experiments and comparison with South Island, New Zealand, *J. Geophys. Res.*, *107*(B7), 2133, doi:10.1029/2001JB000252.

Ranalli, G. (1995), *Rheology of the Earth*, 2nd ed., Chapman and Hall, London.

Ranalli, G., and D. C. Murphy (1987), Rheological stratification of the lithosphere, *Tectonophysics*, *132*, 281–295.

Reddy, S. M., J. Wheeler, R. W. H. Butler, R. A. Cliff, S. Freeman, S. Inger, C. Pickles, and S. P. Kelley (2003), Kinematic reworking and exhumation within the convergent Alpine Orogen, *Tectonophysics*, *365*(1–4), 77–102.

Reinecke, T. (1998), Prograde high- to ultrahigh-pressure metamorphism and exhumation of oceanic sediments at Lago di Cignana, Zermatt-Saas Zone, western Alps, *Lithos*, *42*, 147–189.

Ring, U. and M. T. Brandon (1999), Ductile deformation and mass loss in the Fransiscan Subduction Complex: Implications for exhumation processes in accretionary wedges, in *Exhumation Processes: Normal Faulting, Ductile Flow and Erosion*, edited by U. Ring et al., *Geol. Soc. Spec. Publ. London*, *154*, 55–86.

Rosenbaum, G., and G. S. Lister (2005), The western Alps from the Jurassic to Oligocene: Spatio-temporal constraints and evolutionary reconstructions, *Earth Sci. Rev.*, *69*, 281–306.

Royden, L. H. (1993), The steady state thermal structure of eroding orogenic belts and accretionary prisms, *J. Geophys. Res.*, *98*(B3), 4487–4507.

Rubatto, D., and J. Hermann (2001), Exhumation as fast as subduction?, *Geology*, *29*(1), 3–6.

Rudolph, M. L., T. V. Gerya, D. A. Yuen, and S. DeRosier (2004), Visualization of multiscale dynamics of hydrous cold plumes at subduction zones, *Visual Geosci.*, *17*, doi:10.1007/s10069-004-0017-2.

Scaillet, S. (1996), Excess ^{40}Ar transport scale and mechanism in high-pressure phengites: A case study from an eclogitized metabasite of the Dora Maira nappe, western Alps, *Geochim. Cosmochim. Acta*, *60*, 1075–1090.

Schwartz, S. (2002), La zone Piémontaise des Alpes Occidentales: Un paléo-complexe de subduction, BRGM thesis, Univ. Claude Bernard Lyon 1, Lyon, France.

Schwartz, S., J. M. Lardeaux, S. Guillot, and P. Tricart (2000a), Diversité du métamophisme éclogitique dans le massif ophiolitique du Monviso (Alpes occidentales, Italie), *Geodinam. Acta*, *13*, 169–188.

Schwartz, S., J. M. Lardeaux, and P. Tricart (2000b), La zone d'Acceglio (Alpes cottiennes): Un nouvel exemple de croûte continentale éclogitisée dans les Alpes occidentales, *Compte rendu de l'académie des Sciences de Paris*, *330*, 859–866.

Schwartz, S., P. Allemand, and S. Guillot (2001), Numerical model of the effect of serpentinites on the exhumation of eclogitic rocks: Insights from the Monviso ophiolitic massif (western Alps), *Tectonophysics*, *342*, 193–206.

Shea, W. T., and A. K. Kronenberg (1992), Rheology and deformation mechanisms of an isotropic mica schist, *J. Geophys. Res.*, *97*(B11), 15,201–15,237.

Shreve, R. L., and M. Cloos (1986), Dynamics of sediment subduction, melange formation, and prism accretion, *J. Geophys. Res.*, *91*(B10), 10,229–10,245.

Spalla, M. I., J. M. Lardeaux, G. V. Dal Piaz, G. Gosso, and B. Messiga (1996), Tectonic significance of Alpine eclogites, *J. Geodynam.*, *21*(3), 257–285.

Spear, F. S. (1993), *Metamorphic Phase Equilibria and Pressure-Temperature-Time Paths*, 800 pp., Mineral. Soc. of Am., Washington, D. C.

Stampfli, G. M., J. Mosar, D. Marquer, R. Marchant, T. Baudin, and G. D. Borel (1998), Subduction and obduction processes in the Swiss Alps, *Tectonophysics*, *296*, 159–204.

Stöckhert, B., and T. V. Gerya (2005), Pre-collisional high pressure metamorphism and nappe tectonics at active continental margins: A numerical simulation, *Terra Nova*, *17*(2), 102–110.

Todd, C. S., and M. Engi (1997), Metamorphic field gradients in the central Alps, *J. Metamorph. Geol.*, *15*, 513–530.

Toussaint, G., E. Burov, and J. P. Avouac (2004), Tectonic evolution of a continental collision zone: A thermomechanical numerical model, *Tectonics*, *23*, TC6003, doi:10.1029/2003TC001604.

Tsujimori, T., V. B. Sisson, J. G. Liou, G. E. Harlow, and S. S. Sorensen (2006), Very-low-temperature record of the subduction process: A review of worldwide lawsonite eclogites, *Lithos*, *92*(3), 609–624.

Turcotte, D. L. and G. Schubert (2002), *Geodynamics*, 2nd ed., 456 pp., Cambridge Univ. Press, Cambridge.

Vanderhaeghe, O., S. Medvedev, P. Fullsack, C. Beaumont, and R. A. Jamieson (2003), Evolution of orogenic wedges and continental plateaus: Insights from thermal-mechanical models with subduction basal boundary conditions, *Geophys. J. Int.*, *153*(1), 27–51.

Van der Klauw, S. N. G. C., T. Reinecke, and B. Stöckhert (1997), Exhumation of ultrahigh-pressure metamorphic oceanic crust from Lago di Cignana, Piemontese zone, western Alps: The structural record in metabasites, *Lithos*, *41*, 79–102.

Vasilyev, O. V., T. V. Gerya, and D. A. Yuen (2004), The application of multidimensional wavelets to unveiling multi-phase diagrams and in situ physical properties of rocks, *Earth Planet. Sci. Lett.*, *223*, 49–64.

Vidal, O., and T. Parra (2000), Exhumation paths of high pressure metapelites obtained from local equilibria for chlorite-phengite assemblages, *Geol. J.*, *35*, 139–161.

Villa, I. M. (1998), Isotopic closure, *Terra Nova*, *10*, 42–47.

Wakabayashi, J. (1990), Counterclockwise P-T-t paths from amphibolites, Franciscan Complex, California: Relics from the early stages of subduction zone metamorphism, *J. Geol.*, *98*, 657–680.

Widmer, T., and A. B. Thompson (2001), Local origin of high pressure vein material in eclogite facies rocks of the Zermatt-Saas Zone, Switzerland, *Am. J. Sci.*, *301*, 627–656.

Willet, S. D. (1999), Orogeny and orography: The effects of erosion on the structure of mountain belts, *J. Geophys. Res.*, *104*(B12), 28,957–28,981.

Zeitler, P. K., et al. (2001), Erosion, Himalayan geodynamics, and the geology of metamorphism, *GSA Today*, *11*, 4–8.

P. Agard, E. Burov, L. Jolivet, L. Le Pourhiet, C. Tiberi, and P. Yamato, Laboratoire de Tectonique, UMR CNRS 7072, Université Paris 6, Case 129, Tour 46-0, 2E, 4 pl. Jussieu, 75252 Paris Cedex 05, France. (philippe.yamato@lgs.jussieu.fr)